

Non-parametric regression for robot learning on manifolds

López-Custodio, P.C.^{*1}, Bharath, K.², Kucukyilmaz, A.¹, Preston, S.P.²

¹School of Computer Science, University of Nottingham

²School of Mathematical Sciences, University of Nottingham

{pablo.lopez-custodio, karthik.bharath, ayse.kucukyilmaz, simon.preston}@nottingham.ac.uk

Abstract—Many of the tools available for robot learning were designed for Euclidean data. However, many applications in robotics involve manifold-valued data. A common example is orientation; this can be represented as a 3-by-3 rotation matrix or a quaternion, the spaces of which are non-Euclidean manifolds. In robot learning, manifold-valued data are often handled by relating the manifold to a suitable Euclidean space, either by embedding the manifold or by projecting the data onto one or several tangent spaces. These approaches can result in poor predictive accuracy, and convoluted algorithms. In this paper, we propose an “intrinsic” approach to regression that works directly within the manifold. It involves taking a suitable probability distribution on the manifold, letting its parameter be a function of a predictor variable, such as time, then estimating that function non-parametrically via a “local likelihood” method that incorporates a kernel. We name the method kernelised likelihood estimation. The approach is conceptually simple, and generally applicable to different manifolds. We implement it with three different types of manifold-valued data that commonly appear in robotics applications. The results of these experiments show better predictive accuracy than projection-based algorithms.

I. INTRODUCTION

In recent years, learning from demonstration (LfD) has become an essential approach in robotics research. LfD has been particularly useful for imitating complex human motion which is difficult to mimic by trajectory planning algorithms. Instead, in LfD, the user teaches the robot to follow a trajectory by means of a series of demonstrations.

In this context, Dynamic Movement Primitives (DMP) [1] were introduced to learn a linear attractor system that follows a demonstration. However, in many applications, it is also desired to learn a probability distribution from a series of demonstrations. Encoding how “important” a point is, due to the variability of the demonstrations around it, is crucial in optimal control [2]. This sense of variability can also be exploited to regulate the stiffness of the robot when it interacts with humans [3], to avoid new obstacles [4], or to detect intentions in shared control [5]. Hence, probabilistic approaches have been proposed including Gaussian Mixture Regression (GMR) [6], [7], Probabilistic Movement Primitives (ProMP) [8], and Kernelised Movement Primitives (KMP) [9].

All these LfD methods rely on the multivariate normal distribution as the probabilistic model, and thus only work with Euclidean data. This is not a problem when working in joint space. However, in many applications, working in task space

is more convenient. Working in task space aids awareness of the environment, facilitating obstacle avoidance and adaptation to changes. Working in task space is also convenient when learning human skills as it is possible to track objects or parts of the human body. Then these trajectories are transferable to different robots, whilst in joint-space learning, they are exclusive to the robot used for the demonstrations.

However, the problem of not being able to represent orientations in Euclidean space poses a big challenge since the above-mentioned LfD methods are no longer suitable for the training data. A tempting fix is to work with Euler angles. However, since these are three directions, rather than three real numbers, the search space is \mathbb{T}^3 , which is still non-Euclidean. Even worse, the gimbal-lock singularity means an infinity of triads can represent the same orientation which is a major problem for a probabilistic treatment.

Unfortunately, orientations in task space are not the only type of non-Euclidean data encountered in robotics applications. Any data assuming values in a set where Euclidean geometry of vector spaces is not available is said to be non-Euclidean, and in robotic applications the set can usually be modelled as a smooth manifold. Other examples of manifold-valued data in robotics include: the direction of a table-top grasp (Fig. 1 top-left), the direction of a cutting tool as end-effector (Fig. 1 top-right), the line defining a pointing action, the stiffness matrix of the robot, and the force and velocity manipulability ellipsoids (Fig. 1 bottom).

A common way to tackle the problem of working with manifold-valued data is through an embedding. Take for example data $\{\mathbf{x}_i\}_{i=1}^N$, where \mathbf{x}_i are unit quaternions, so, per notation of Sec. II-A, $\mathbf{x}_i \in \mathcal{S}^3/\mathbb{Z}_2$. If a “mean orientation” is of interest, the data is treated as Euclidean and the familiar arithmetic mean $N^{-1} \sum_i \mathbf{x}_i$ is evaluated. This results in a value in \mathbb{R}^4 that is not a unit quaternion. This can be remedied by renormalising, since $\sum_i \mathbf{x}_i / \|\sum_i \mathbf{x}_i\|$ is a “mean” that is indeed in the manifold. This is a simple example of what is sometimes called an *extrinsic*, or *embedding*, approach that embeds the manifold into a higher-dimensional Euclidean space, exploits the linear structure of that embedding space, then employs a projection mapping back into the manifold [3]. Extrinsic approaches such as this can work well, especially when the goal is to compute a point-wise quantity such as a mean, but for general manifolds there is not always a natural choice of embedding, nor way to characterise dispersion, and in some settings—such as when the data are highly dispersed

^{*}Corresponding author.

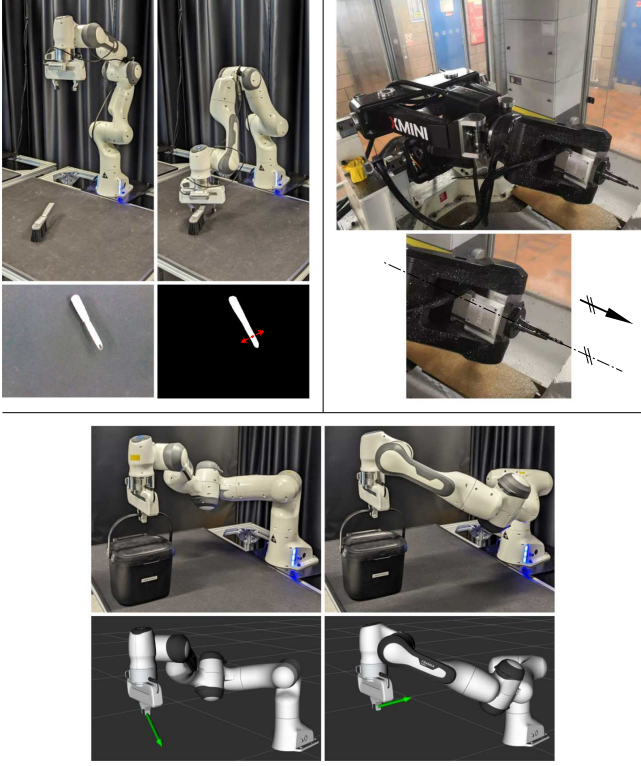


Fig. 1. Examples of manifold-valued data in robotics. TOP-LEFT: A top-table grasp is an element of $\mathbb{R}^3 \times S^1$ which in this case parametrises the Schoenflies group of displacements, $X(4)$. TOP-RIGHT: The orientation of the cutting tool of the 5-DOF Exechon XMini robot [10] is a direction in S^2 . BOTTOM: The 7-DOF Franka Panda robot lifts a box in two different configurations but the same pose of end-effector. The direction of maximum force achievable is shown for each configuration. This direction is found by computation of the manipulability ellipsoid, an element of the manifold of SPD matrices, $\text{Sym}^+(6)$

on the manifold—estimators can behave erratically.

A different approach to analyse manifold-valued data is to employ *tangent space* projections. This involves picking a point on the manifold, known as the base, and using the inverse exponential map to project the data from the manifold to the tangent plane of the base, which is a Euclidean space where standard tools can then be used. Adequacy of the approach depends on two inter-related considerations: dispersion in the data around the base, and curvature of the manifold. Linearising the data through tangent space projections works well when dispersion is small and curvature of the manifold does not appreciably distort distances of points far from the base; when dispersion is large, the approach is suitable only when curvature of the manifold is non-positive everywhere. Large dispersion will result in distorted estimation of the dispersion structure of the projected data points on the tangent space of the base. To see this, consider the top of Fig. 2 which shows a data set on the unit sphere, S^2 . This data has been simulated from a distribution with mean $\mu = (0, 0, 1)$. Using the inverse exponential map, the data is projected onto a tangent plane at μ , and a normal distribution is fitted there. The obtained covariance matrix has eigenvalues $(0.0506, 0.004)$. Now we rotate the data so they are further away from the tangent point (mimicking data from some “extreme” part of

a set of trajectories) as shown at the bottom part of Fig. 2. The data is projected onto the same tangent space as before and a new normal distribution is fitted. The new eigenvalues are $(0.198, 0.0354)$, significantly larger than before and with different proportion.

Positively curved manifolds cannot be linearised through a single tangent space, and projections using the inverse exponential map are only locally well-defined. An important positively curved manifold that arises in robotics is the quotient manifold S^3/\mathbb{Z}_2 of orientations used to represent three-dimensional rotations as quaternions with antipodal symmetry, where $x \in S^3$ and $-x \in S^3$ represent the same rotation.

Relatedly, the Riemannian Gaussian distribution [11], [12] is commonly used in probabilistic modelling of manifold-valued data. The distribution is the image under the exponential map of a Gaussian distribution defined on the tangent space of a chosen base point, and operationally amounts to fitting a multivariate normal distribution to data projected onto the tangent space of the base point. Again, curvature of the manifold plays an important role in its definition: for positively curved manifolds, support of the Gaussian distribution on the tangent space is restricted to a suitable subset, while no restrictions are required for non-positively curved manifolds. These distributions have been profitably used for manifold-valued data in robotics [13]–[20].

The above-mentioned issues for tangent space projections are exacerbated for data from trajectories on manifolds, since trajectories typically span larger subsets of the manifold, especially when considering one single tangent space [13], [14]. In these cases, curvature effects become more pronounced, and data analysis based on tangent space projections can lead to unreliable conclusions. Notwithstanding these issues, adaptation of trajectory learning methods to manifold-valued data has been done relying on tangent-space projections¹. These include the adaptations of ProMP [24] and KMP [13] to orientational data, and GMR to general Riemannian manifolds [15], [17]

Due to the problems arising from data projection, in this paper we present an alternative method for robot learning that works directly on the manifold. Hence, we say that our method is *intrinsic*. Our approach exploits the idea of non-parametric regression, which remains largely unexplored in on-manifold robot learning research. In addition, we build upon probability distribution models that are rarely or never used in the robotics field. For example, we make use of the Angular Central Gaussian (ACG) distribution for axial data as a less computationally expensive alternative to the Bingham distribution [25], [26], whose computational complexity makes it unappealing for robotics applications, although it has been used in the pose estimation problem [27] and in reinforcement learning [28]. Our approach is based on the idea of *local likelihood* [29], [30], where regression is done by incorporating kernel weights into the terms of a log-likelihood expression. By this means, we are able to incorporate probability distributions tailored to the data structure in a regression model that relates a predictor

¹The adaptation of DMP to orientations [21]–[23] does not require tangent-space projections since it does not provide a probabilistic model.

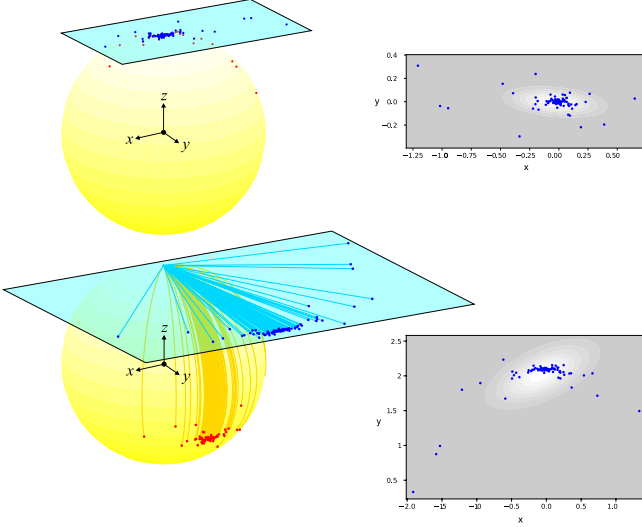


Fig. 2. TOP: a dataset (red) on the unit sphere, \mathcal{S}^2 , and its projection (blue) onto a tangent plane at $(0, 0, 1)$ where the data are centred. BOTTOM: the same data rotated $-2\pi/3$ about x so they are more distant from $(0, 0, 1)$. These data projected onto the same tangent plane at $(0, 0, 1)$ show how the dispersion structure and hence fitted normal distribution become distorted.

variable to a manifold-valued response. We call our approach *kernelised likelihood estimation*.

The advantages of our approach are the following:

- The algorithm is simple. The steps can be summarised in a maximization of a weighted sum of terms. This contrasts with other methods whose complexity stems from the adaptation of Euclidean-designed algorithms to manifold-valued data.
- As it will be shown in the experiments section, by working intrinsically on the manifold, the estimation is more precise compared to methods that work on the tangent bundle.
- The intrinsic nature of the estimation method ensures that it can be used for data on both positively and nonpositively curved manifolds.
- Both trajectory learning and regression can be carried out with the same algorithm.
- No joint distributions between predictor (input) and response (output) are defined. The shape of the covariance of these joint distributions is affected if either predictor or response are re-scaled, for example, due to a change of units.
- The predictor is not limited to scalars, it can also be manifold-valued.
- In the case of trajectory learning, adaptation to via-points (both at the end and in the middle of the trajectory) is simple.
- A method for generating random trajectories from the learnt model is presented. This method reuses the same idea of kernelised likelihood.
- Unlike parametric models in which the model complexity is constrained by the parametrisation, the approach we propose incorporates non-parametric estimation, allowing the model to get more flexible as the amount of training data grows.

Model flexibility comes at the cost of new predictions having to depend directly on the training data (rather than some low-dimensional parameter vector); this is a potential disadvantage, though one shared by any non-parametric method.

In this paper, it is assumed that a task-space controller is available. Therefore, we only focus on the learning and generation of trajectories but not on the design of controllers.

This paper is organised as follows: Section II provides an overview of common manifold-valued data in robotics. Section III defines the problem statement to be tackled in this paper. Section IV introduces the method we propose to solve this problem. In this method, a suitable probability distribution model is needed, hence, Section V presents several previously introduced models for different types of manifold-valued data. The proposed method is then tested in a series of experiments presented in Section VI. Finally, conclusions are drawn in Section VII.

The related source code will be made public upon acceptance of the paper.

II. COMMON EXAMPLES OF MANIFOLD-VALUED DATA IN ROBOTICS

Manifold-valued data appears in a multitude of applications in robotics. A list of these manifolds is summarised by [31]. Although the method presented in this paper works for any of those manifolds, we focus on the ones introduced in this Section, as these are some of the most commonly encountered manifolds in robotics applications.

A. Directions, \mathcal{S}^{d-1}

Directions lie on the unit sphere $\mathcal{S}^{d-1} := \{\mathbf{x} | \mathbf{x}^\top \mathbf{x} = 1, \mathbf{x} \in \mathbb{R}^d\}$. An example of directional data is the orientation of a rotating cutting tool (Fig. 1, top-right), which is an element of \mathcal{S}^2 . Similarly, the orientation of a table-top grasp is an angle in \mathcal{S}^1 (Fig. 1, top-left), while the whole grasp, including position, is in $\mathbb{R}^3 \times \mathcal{S}^1$. Since the angle is always measured about an axis whose direction is constant, grasps belong to the 4-dimensional group of *Schoenflies* displacements, $X(4)$ [32]. Other examples of data belonging to the $X(4)$ group include the end-effector poses of the Delta and the SCARA robots.

B. Axes, $\mathcal{S}^d/\mathbb{Z}_2$

In the manifold of axes, $\mathcal{S}^{d-1}/\mathbb{Z}_2$, $\mathbf{x} \in \mathcal{S}^{d-1}$ and its antipodal direction $-\mathbf{x}$ represent the same element. There are plenty of applications involving axial data, but an additional reason that $\mathcal{S}^{d-1}/\mathbb{Z}_2$ is so important is that it is isomorphic to the special orthogonal group, $SO(3)$, defined in the following section. Therefore, methods devised for $\mathcal{S}^3/\mathbb{Z}_2$ can be used directly for applications involving orientational data.

C. Orientations, the special orthogonal group, $SO(3)$; and poses, the special Euclidean group, $SE(3)$

The special orthogonal group of dimension 3, $SO(3)$, is defined as the set of orthogonal matrices of determinant 1. These correspond to rotation matrices in 3-dimensional space.

Hence, the orientation of any rigid body can be represented by an element of $\text{SO}(3)$.

Consider the map $\mathbf{R} : \mathcal{S}^3 \rightarrow \text{SO}(3)$ defined as:

$$\mathbf{R}(\mathbf{x}) := \mathbf{I}_3 + 2x_1 \text{skew}(x_2, x_3, x_4) + 2 \text{skew}(x_2, x_3, x_4)^2 \quad (1)$$

where $\mathbf{x} := (x_1, x_2, x_3, x_4)^\top \in \mathcal{S}^3$, and

$$\text{skew}(v_1, v_2, v_3) := \begin{pmatrix} 0 & -v_3 & v_2 \\ v_3 & 0 & -v_1 \\ -v_2 & v_1 & 0 \end{pmatrix}.$$

$\mathbf{R}(\cdot)$ is surjective, however $\mathbf{R}(\mathbf{x}) = \mathbf{R}(-\mathbf{x})$, $\forall \mathbf{x} \in \mathcal{S}^3$. Due to this antipodal redundancy, $\text{SO}(3)$ is isomorphic to $\mathcal{S}^3/\mathbb{Z}_2 \cong P\mathbb{R}^3$. In kinematics, (1) provides a map between rotation matrices and unit quaternions.

The Special Euclidean group in 3-dimensional space, $\text{SE}(3)$, is the set of rigid-body transformations. It is a Lie group, hence, it allows for a Lie algebra, $\text{se}(3)$. $\text{SE}(3)$ can be identified with the semidirect product $\text{SE}(3) = \text{SO}(3) \ltimes \mathbb{R}^3$.

The pose (position and orientation) of the end-effector of a robot with respect to a fixed coordinate system is a rigid body transformation and thus an element of $\text{SE}(3)$. Therefore, for a task-space trajectory, the data are $\{(\mathbf{X}_i, t_i)\}_i^N$, where $\mathbf{X}_i \in \text{SE}(3)$ is a 4-by-4 transformation matrix, a dual quaternion, or an element of any other parametrisation of $\text{SE}(3)$.

For many applications, it is reasonable to work with position and orientation independently. Therefore, the task-space trajectory $\{(\mathbf{X}_i, t_i)\}_i^N$ can be represented as $\{(\mathbf{x}_i, \mathbf{p}_i, t_i)\}_i^N$, where $\mathbf{x}_i \in \mathcal{S}^3/\mathbb{Z}_2$ is an orientation, and $\mathbf{p}_i \in \mathbb{R}^3$, a position.

D. Symmetric positive definite matrices, $\text{Sym}^+(d)$

The set of symmetric positive definite (SPD) matrices is defined as $\text{Sym}^+(d) := \{\mathbf{M} \in \text{Sym}(d) \mid \mathbf{x}^\top \mathbf{M} \mathbf{x} > 0 \forall \mathbf{x} \in \mathbb{R}^d\}$.

Although data in $\text{Sym}^+(d)$ appear in several robotics applications like stiffness and distance covariance matrices, we now explain one of the most important applications of $\text{Sym}^+(d)$ in robot arms: the velocity and force manipulability ellipsoids.

Let $\mathbf{q} \in \mathbb{T}^r$ be the vector of joint angles of a robot arm with r degrees of freedom (DOF). If the end-effector can move in a d -dimensional submanifold of $\text{SE}(3)$, then its velocity $\mathbf{v} \in \mathbb{R}^d$ is related to the joint velocities by $\mathbf{v} = \mathbf{J}(\mathbf{q})\dot{\mathbf{q}}$, while the output wrench $\mathbf{f} \in \mathbb{R}^d$ is related to the joint torques $\boldsymbol{\tau} \in \mathbb{R}^r$ by $\boldsymbol{\tau} = \mathbf{J}^\top(\mathbf{q})\mathbf{f}$. The matrix $\mathbf{J}(\mathbf{q}) \in \mathbb{R}^{d \times r}$ is the *Jacobian matrix* of the robot at configuration \mathbf{q} .

It is possible to use $\mathbf{J}(\mathbf{q})$ to evaluate the performance of the robot at configuration \mathbf{q} [33]. One of such performance indexes evaluates the velocities of the end-effector that can be generated by the set of joint velocities of magnitude one, $\dot{\mathbf{q}}^\top \dot{\mathbf{q}} = 1$ at \mathbf{q} . If $r > d$, replacing the least-squares solution to $\mathbf{v} = \mathbf{J}(\mathbf{q})\dot{\mathbf{q}}$, $\dot{\mathbf{q}} = \mathbf{J}^\top(\mathbf{q})(\mathbf{J}(\mathbf{q})\mathbf{J}^\top(\mathbf{q}))^{-1}\mathbf{v}$, in $\dot{\mathbf{q}}^\top \dot{\mathbf{q}} = 1$ gives:

$$\mathbf{v}^\top (\mathbf{J}(\mathbf{q})\mathbf{J}^\top(\mathbf{q}))^{-1} \mathbf{v} = 1. \quad (2)$$

Define $\mathbf{M}(\mathbf{q}) := \mathbf{J}(\mathbf{q})\mathbf{J}^\top(\mathbf{q}) \in \text{Sym}^+(d)$, and let $\{\lambda_i\}_{i=1}^d$ be its eigenvalues in descending order with corresponding eigenvectors $\{\mathbf{b}_i\}_{i=1}^d \subset \mathcal{S}^{d-1}$. Then (2) defines an ellipsoid whose axes are parallel to $\{\mathbf{b}_i\}_{i=1}^d$ and have lengths $\{1/\sqrt{\lambda_i}\}_{i=1}^d$.

Hence, $\mathbf{v}^\top (\mathbf{M}(\mathbf{q}))^{-1} \mathbf{v} = 1$ is known as the *velocity manipulability ellipsoid* at \mathbf{q} . Equivalently, $\mathbf{f}^\top \mathbf{M}(\mathbf{q})\mathbf{f} = 1$ provides a *force manipulability ellipsoid*.

III. PROBLEM STATEMENT

In the probabilistic trajectory-learning problem, it is desired to predict a variable (response) for a new input (predictor) given a training dataset representing a series of human demonstrations. It is also required to know the variability of the demonstrations for any value of the predictor. We consider the cases in which either the response or both the response and the predictor lie on a manifold.

In the case of scalar predictor and response in a manifold \mathcal{M} , the training data $\mathcal{D} = \{(\mathbf{x}_{ij}, t_{ij})\}_{j=1}^{M_i} \}_{i=1}^N$, $\mathbf{x}_{ij} \in [0, 1]$, $\mathbf{x}_{ij} \in \mathcal{M}$, is a set of N trajectories recorded from human demonstrations, each trajectory i contains M_i data points. Let $P_{\mathcal{M}}(\theta)$ be a probability distribution on \mathcal{M} with parameter(s) θ , so that the mean and dispersion structure are directly or indirectly included in θ . Then, it is desired to estimate $\hat{\theta}(t)$, for any $t \in [0, 1]$. So, we can obtain a trajectory of L points, $\{\theta_k, t_k\}_{k=1}^L$, $\theta_k := \hat{\theta}(t_k)$.

It is also desired to solve the problem of simple regression. In this case, given a new value of the predictor, the value of the response is estimated based on a training dataset. Hence, the training data set is $\mathcal{D} = \{(\mathbf{x}_i, \mathbf{t}_i)\}_{i=1}^N$, $\mathbf{x}_i \in \mathcal{M}_O$, $\mathbf{x}_i \in \mathcal{M}_I$, where \mathcal{M}_I and \mathcal{M}_O are the manifolds of the predictor and response, respectively. The goal is now to estimate $\hat{\mathbf{x}} \in \mathcal{M}_O$ for a new $\mathbf{t} \in \mathcal{M}_I$.

IV. ROBOT LEARNING VIA KERNELISED LIKELIHOOD ESTIMATION

The approach we develop in this paper extends upon the idea of Nadaraya–Watson kernel regression [34], [35], a non-parametric approach that estimates the response variable for a predictor query point as weighted combinations of the training response cases, with weights chosen according to proximity of predictor values. While Nadaraya–Watson regression is appropriate for Euclidean-valued response data, our approach is appropriate for manifold-valued response data and hence to the problems described in Section III. Furthermore, Nadaraya–Watson regression is usually geared towards computing a point estimate, such as a mean, for each value of the predictor, whereas here we are interested too in estimating the dispersion structure.

A. Nadaraya–Watson regression in Euclidean space

Consider training data $\mathcal{D} = \{(x_i, t_i)\}_{i=1}^N$, $x_i, t_i \in \mathbb{R}$. The Nadaraya–Watson estimator of the mean response as a function of the predictor is

$$\hat{\mu}(t) = \sum_{i=1}^N \left[\frac{K_h(t - t_i)}{\sum_{i=1}^N K_h(t - t_i)} x_i \right], \quad (3)$$

where $K_h(t)$ is a non-negative-valued kernel function with bandwidth parameter $h > 0$, a maximum at $t = 0$, and

$\int K_h(t)dt$ equal to a constant independently of h . The value of h sets a trade-off between fitting and smoothness. A commonly used kernel is defined as $K_h(t) := \exp(-t^2/2h^2)$.

Writing (3) as

$$\hat{\mu}(t) = \sum_{i=1}^N W_i(t) x_i, \quad (4)$$

emphasises that the estimator is a simple weighted linear combination of the training response data, with the weight

$$W_i(t) := \frac{K_h(t - t_i)}{\sum_{i=1}^N K_h(t - t_i)}. \quad (5)$$

B. Kernelised likelihood estimation

The Nadaraya–Watson estimator (4) is appealing because it is intuitive and simple to compute. However, it does not generalise directly to manifold-valued response data, $\mathbf{x}_i \in \mathcal{M}$, because weighted combinations of \mathbf{x}_i do not in general lie in \mathcal{M} . Instead, consider first a probability distribution $P_{\mathcal{M}}(\theta)$ defined on the manifold \mathcal{M} , with probability density function $f(\mathbf{x}; \theta)$ and parameter(s) θ , and write

$$X \sim P_{\mathcal{M}}(\theta). \quad (6)$$

Given a sample of data $\{\mathbf{x}_i\}_{i=1}^N$ assumed to be realisations of (6) independent of each other and from t_i , parameter θ can be estimated from the data by maximum likelihood estimation (MLE). The MLE of θ is the maximiser of the log-likelihood:

$$\hat{\theta} = \arg \max_{\theta} \sum_{i=1}^N \log f(\mathbf{x}_i; \theta). \quad (7)$$

In this paper, instead of the data being independent they are of the paired form $\{(\mathbf{x}_i, t_i)\}_{i=1}^N$, and the goal is to predict how the response variable \mathbf{x}_i depends on the predictor t_i . To this end we consider models of the form:

$$(X|T = t) \sim P_{\mathcal{M}}(\theta(t)). \quad (8)$$

This is still somewhat general, because it remains to specify how $\theta(t)$ depends on t . We impose this dependence by prescribing

$$\hat{\theta}(t) = \arg \max_{\theta} \sum_{i=1}^N W_i(t) \log f(\mathbf{x}_i; \theta), \quad (9)$$

where $W_i(t)$ is as defined in (5). This is maximising a “local likelihood” in the sense of [30]. Reflecting how the local likelihood incorporates kernel weights, we call our approach *kernelised likelihood estimation* (KLE).

Once an estimate $\hat{\theta}(t)$ is computed from training data then, by (8), an estimate of $\mathbb{E}(X|T = t)$ is

$$\hat{\mu}(t) = \mathbb{E}(P_{\mathcal{M}}(\hat{\theta}(t))), \quad (10)$$

where \mathbb{E} denotes expectation. Thus, $\hat{\mu}(t)$ defines a smooth path through the training data and, in this sense, provides a solution to the on-manifold regression problem.

For the problem of trajectories on manifolds with training data $\mathcal{D} = \{(\mathbf{x}_{ij}, t_{ij})\}_{j=1}^{M_i} \}_{i=1}^N$, $\mathbf{x}_{ij} \in [0, 1]$, $\mathbf{x}_{ij} \in \mathcal{M}$, we simply rewrite Eq. (9) as:

$$\hat{\theta}(t) = \arg \max_{\theta} \sum_{i=1}^N \sum_{j=1}^{M_i} W_{ij}(t) \log f(\mathbf{x}_{ij}; \theta), \quad (11)$$

where

$$W_{ij}(t) := \frac{K_h(t - t_{ij})}{\sum_{i=1}^N \sum_{j=1}^{M_i} K_h(t - t_{ij})}. \quad (12)$$

To illustrate the application of the KLE method, consider the following scenarios with scalar, Euclidean and manifold-valued data:

Scalar response: Consider the case of $x_i, t_i \in \mathbb{R}$ (that is, let \mathcal{M} be \mathbb{R}), let $P_{\mathcal{M}}(\theta)$ with $\theta = \{\mu, \sigma^2\}$ be the normal distribution $\mathcal{N}(\mu, \sigma^2)$. Then, by Eq. (9), $\hat{\theta}(t) = \{\hat{\mu}(t), \hat{\sigma}^2(t)\}$, where

$$\hat{\mu}(t) = \sum_{i=1}^N W_i(t) x_i, \quad \hat{\sigma}^2(t) = \sum_{i=1}^N W_i(t) [x_i - \hat{\mu}(t)]^2. \quad (13)$$

Thus in this case the estimator of the mean, $\hat{\mu}(t)$, is exactly the Nadaraya–Watson estimator (4). This approach further provides an estimate of how the variance, σ^2 , varies with the predictor, t .

Euclidean response: Now consider $\mathcal{D} = \{(\mathbf{x}_{ij}, t_{ij})\}_{j=1}^{M_i} \}_{i=1}^N$, $\mathbf{x}_{ij} \in \mathbb{R}^d$, $t_{ij} \in [0, 1]$ (that is, let \mathcal{M} be \mathbb{R}^d), and let $P_{\mathcal{M}}(\theta)$ with $\theta = \{\boldsymbol{\mu}, \boldsymbol{\Sigma}\}$ be the multivariate normal distribution $\mathcal{N}(\boldsymbol{\mu}, \boldsymbol{\Sigma})$. Then $\hat{\theta}(t) = \{\hat{\boldsymbol{\mu}}(t), \hat{\boldsymbol{\Sigma}}(t)\}$, where

$$\begin{aligned} \hat{\boldsymbol{\mu}}(t) &= \sum_{i=1}^N \sum_{j=1}^{M_i} W_{ij}(t) \mathbf{x}_{ij}, \\ \hat{\boldsymbol{\Sigma}}(t) &= \sum_{i=1}^N \sum_{j=1}^{M_i} \left[W_{ij}(t) (\mathbf{x}_{ij} - \hat{\boldsymbol{\mu}}(t)) (\mathbf{x}_{ij} - \hat{\boldsymbol{\mu}}(t))^{\top} \right], \end{aligned} \quad (14)$$

where the weights $W_{ij}(t)$ Eq. (12). The proof of Eq. (14) is given in Appendix A.

Manifold-valued response: To illustrate the application of the KLE method to on-manifold trajectory learning, consider the pseudocode in Algorithm 1. In this case, $\mathcal{D} = \{(\mathbf{x}_{ij}, t_{ij})\}_{j=1}^{M_i} \}_{i=1}^N$, $\mathbf{x}_{ij} \in \mathcal{S}^{d-1}/\mathbb{Z}_2$, $t_{ij} \in [0, 1]$, that is, \mathcal{M} is $\mathcal{S}^{d-1}/\mathbb{Z}_2$. To model the data, an ACG distribution (with parameter Λ) is used. This, and other models of distributions on manifolds, are explained in detail in Section V. In Algorithm 1, the function `Ker_MLE_ACG` can be replaced by the corresponding solution to the KLE in Eq. (9) for a probability distribution that is suitable for the data. Many models admit a simple solution for Eq. (9). It will be seen in Section V that for the ACG distribution on $\mathcal{S}^{d-1}/\mathbb{Z}_2$, and for the Lognormal distribution on $\text{Sym}^+(d)$, such a solution simplifies to Eq. (20), and Eqs. (26) and (27), respectively. However, it will be seen that for the ESAG distribution on \mathcal{S}^{d-1} no simplified expression is known, and hence, Eq. (9) has to be solved with a numerical method. Finally, for the Euclidean case, Eq. (14) give the solution to the maximization of the kernelised likelihood estimation.

It can be seen that Algorithm 1 has a simpler structure than most of the other methods for on-manifold trajectory learning.

Manifold-valued predictor: In the case of a manifold-valued predictor, $\mathbf{t}_{ij} \in \mathcal{M}_I$, Eq. (9) holds with a kernel of the form $K_h(d_{\mathcal{M}_I}(\mathbf{t}, \mathbf{t}_{ij}))$, where $d_{\mathcal{M}_I}(\cdot)$ is a metric on \mathcal{M}_I .

Algorithm 1: Trajectory learning with ACG distribution

```

1 Function Ker_MLE_ACG( $t, \mathcal{D}, h, \varepsilon$ ):
2    $\hat{\Lambda}_{\text{old}} = \mathbf{I}_d$ 
3   do
4      $\hat{\Lambda}_{\text{new}} \leftarrow \text{Eq. (20)}$  // input:  $t, \mathcal{D}, h$ 
5      $E = d_{\text{SPD}}(\hat{\Lambda}_{\text{old}}, \hat{\Lambda}_{\text{new}})$ 
6      $\hat{\Lambda}_{\text{old}} = \hat{\Lambda}_{\text{new}}$ 
7   while  $E < \varepsilon$ 
8 return  $\hat{\Lambda}_{\text{new}}$ 
9
10 Function main( $\mathcal{D}, T, h, \varepsilon$ ):
11   for  $n = 1$  to  $T$  do
12      $t_n = (n - 1)/(T - 1)$ 
13      $\hat{\Lambda}_n = \text{Ker\_MLE\_ACG}(t_n, \mathcal{D}, h, \varepsilon)$ 
14   end
15 return  $\{t_n, \hat{\Lambda}_n\}_{n=1}^T$ 

```

C. Trajectory adaptation to via-points, and blending of trajectories

Consider the simplest case of a scalar trajectories dataset $\mathcal{D} = \{\{(x_{ij}, t_{ij})\}_{j=1}^{M_i}\}_{i=1}^N$, $x_{ij} \in \mathbb{R}$, $t_{ij} \in [0, 1]$. Then $\hat{\mu}(t)$ and $\hat{\sigma}(t)$, $t \in [0, 1]$, can be determined by Eq (13). It is desired to adapt this model so that the trajectories pass through μ^* at t^* with an uncertainty controlled by σ^* .

To adapt this model, we synthetically generate a second dataset $\mathcal{E} = \{\{(y_{ij}, t_{ij})\}_{j=1}^R\}_{i=1}^S$, where for every t_j , a set $\{y_{ij}\}_{i=1}^S$, $y_{ij} \sim \mathcal{N}(\mu^*, \sigma^*)$, is sampled.

Then, the adapted model is obtained as a mixture of \mathcal{D} and \mathcal{E} . The kernels weighting \mathcal{D} and \mathcal{E} are now multiplied by activation functions $\alpha(t)$ and $\beta(t) := 1 - \alpha(t)$, respectively, so that the contributions of the data points are activated or deactivated in the KLE algorithm. Hence, the adapted mean yields:

$$\begin{aligned} \hat{\mu}(t) = & \frac{1}{C(t)} \left[\sum_{i=1}^N \sum_{j=1}^{M_i} \alpha(t_{ij}) K_h(t - t_{ij}) x_{ij} \right. \\ & \left. + \sum_{i=1}^S \sum_{j=1}^R \beta(t_j) K_h(t - t_j) y_{ij} \right], \end{aligned}$$

where

$$\begin{aligned} C(t) = & \sum_{i=1}^N \sum_{j=1}^{M_i} \alpha(t_{ij}) K_h(t - t_{ij}) \\ & + \sum_{i=1}^S \sum_{j=1}^R \beta(t_j) K_h(t - t_j), \end{aligned}$$

where $\alpha(t^*) \approx 0$ and $\beta(t^*) \approx 1$, while $\alpha(t) \approx 1$ and $\beta(t) \approx 0$ for t far away from t^* . The adapted $\hat{\sigma}(t)$ is obtained inserting the same activation functions. Fig. 3 shows an example in which a series of scalar demonstrations are adapted to $\mu^* = 0.6$ at $t^* = 0.7$.

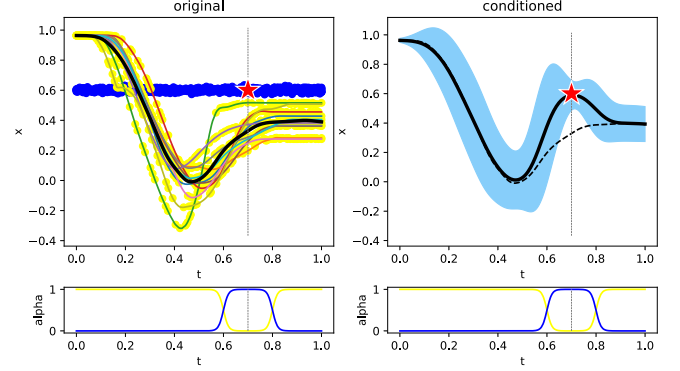


Fig. 3. Adaptation of scalar trajectories to $\mu^* = 0.6$ at $t^* = 0.7$. LEFT: \mathcal{D} (yellow dots) consists of 700 samples taken from 10 demonstrated curves. The resulting $\hat{\mu}(t)$ is shown in thick black curve. \mathcal{E} (blue dots) is generated with $\mu^* = 0.6$ and $\sigma^* = 0.001$. BOTTOM: The activation functions correspond to $\beta(t) = 0.5 \tanh(50(t - t^* + 0.1)) - 0.5 \tanh(50(t - t^* - 0.1))$ and $\alpha(t) = 1 - \beta(t)$. RIGHT: The result of adaptation with the blue area showing $\pm 1.5\hat{\sigma}(t)$.

Since this modification to the KLE algorithm simply acts on the kernels - by weighting them with the activation functions - the same change is applied to the kernels in Eq (9) in order to adapt trajectories on manifolds to new via-points.

The problem of trajectory blending can be solved by the same method by letting the activation functions act on the data points of the two trajectory sets to be blended. In this case, the activation functions are smoothed step functions.

D. Trajectory generation

After $\hat{\theta}(t)$ has been computed for a trajectories dataset $\mathcal{D} = \{\{(x_{ij}, t_{ij})\}_{j=1}^{M_i}\}_{i=1}^N$, $\mathbf{x}_{ij} \in \mathcal{M}$, $t_{ij} \in [0, 1]$, new trajectories can be generated around the mean by re-sampling and smoothing along $t \in [0, 1]$. First, generate a set $\mathcal{D}_r = \{(\mathbf{x}_{r,i}, t_{r,i})\}_{i=1}^{N_r}$, where $\mathbf{x}_{r,i} \sim P_{\mathcal{M}}(\hat{\theta}(t_{r,i}))$. Then, apply the KLE regression from Eq. (9) as a smoother for \mathcal{D}_r . This results in the estimation of the parameter $\hat{\theta}_r(t)$ for \mathcal{D}_r . Then, the generated curve, $\hat{\mu}_r(t)$, is defined by Eq. (10), by taking $\hat{\theta}(t)$ equal to $\hat{\theta}_r(t)$. Consider the special case when \mathcal{M} is \mathbb{R}^d , $P_{\mathcal{M}}$ is the normal distribution, and $\hat{\theta}_r(t)$ in Eq. (10) is treated as random (depending on the sampling distribution of the training data) then $\hat{\mu}_r(t)$ is a Gaussian Process (GP). Hence the proposed approach to trajectory generation is a generalization to \mathcal{M} of a GP model in \mathbb{R}^d ; see Appendix A for further explanation.

E. Autonomous systems

For trajectories in task space, velocities can be learnt as well in order to generate time-independent trajectories. Hence, the training data for an autonomous system is $\mathcal{D} = \{\{(\mathbf{T}_{ij}, \mathbf{V}_{ij}, t_{ij})\}_{j=1}^{M_i}\}_{i=1}^N$, where $\mathbf{T}_{ij} \in \text{SE}(3)$ is a pose and $\mathbf{V}_{ij} \in \text{se}(3)$ a twist. The proposed on-manifold learning

method allows to learn both the position and the orientation parts of \mathbf{T}_{ij} , and since $\text{se}(3)$ is a vector space, \mathbf{V}_{ij} is easy to learn with the same method using the multivariate normal distribution as model (Eq. (14)). Finally, the generated trajectories have the form $\{(\mathbf{T}_n, \mathbf{V}_n)\}_{n=1}^T$. Since $\text{se}(3)$ enjoys of Euclidean structure, the learning of \mathbf{V}_{ij} is not taken into account in the rest of the paper.

V. PROBABILITY DISTRIBUTIONS ON RELEVANT MANIFOLDS

The method described in Section IV requires the use of a probability distribution, $\mathcal{P}_{\mathcal{M}}(\theta)$, on the manifold, \mathcal{M} , where the response variable lies. In this section, we introduce probability distributions relevant to the manifolds introduced in Section II. For each distribution, we present the probability density function and the “standard” MLE solution given independent identically distributed data; then we present the new kernelised solution, that is, the solution of (9), that solves the regression problem involving response data on \mathcal{M} .

A. The elliptically symmetric angular Gaussian distribution on \mathcal{S}^{d-1}

Given $\mathbf{y} \sim \mathcal{N}(\boldsymbol{\mu}, \mathbf{V})$, $\mathbf{y} \in \mathbb{R}^d$, with constraints $\mathbf{V}\boldsymbol{\mu} = \boldsymbol{\mu}$ and $|\mathbf{V}| = 1$, the directions $\mathbf{x} := \mathbf{y}/\|\mathbf{y}\| \in \mathcal{S}^{d-1}$ have an *elliptically symmetric angular Gaussian* (ESAG) distribution with density [36]:

$$f_{\text{ESAG}}(\mathbf{x}; \boldsymbol{\mu}, \mathbf{V}) := \frac{C_d}{(\mathbf{x}^\top \mathbf{V}^{-1} \mathbf{x})^{d/2}} \exp \left[\frac{1}{2} \left\{ \frac{(\mathbf{x}^\top \boldsymbol{\mu})^2}{\mathbf{x}^\top \mathbf{V}^{-1} \mathbf{x}} - \boldsymbol{\mu}^\top \boldsymbol{\mu} \right\} \right] M_{d-1} \left(\frac{\mathbf{x}^\top \boldsymbol{\mu}}{(\mathbf{x}^\top \mathbf{V}^{-1} \mathbf{x})^{1/2}} \right), \quad (15)$$

where $C_d := 1/(2\pi)^{(d-1)/2}$ and, for $d = 2$ and 3 , respectively:

$$\begin{aligned} M_1(\alpha) &:= \alpha \Phi(\alpha) + \phi(\alpha), \\ M_2(\alpha) &:= (1 + \alpha^2) \Phi(\alpha) + \alpha \phi(\alpha), \end{aligned}$$

where $\phi(\cdot)$ and $\Phi(\cdot)$ are the functions for standard normal probability density and cumulative density, respectively. See [36] for M_{d-1} with $d > 3$.

Let $0 \leq \rho_1 \leq \dots \leq \rho_d = 1$ be the eigenvalues of \mathbf{V} with corresponding eigenvectors $\boldsymbol{\xi}_1, \dots, \boldsymbol{\xi}_d$, where $\boldsymbol{\xi}_d = \boldsymbol{\mu}/\|\boldsymbol{\mu}\|$. Then the mean of the distribution is $\boldsymbol{\xi}_d$ while $\|\boldsymbol{\mu}\|$ controls the concentration. The rest of the eigenvectors represent the axes of symmetry of the elliptical contours.

For $d = 3$, the ESAG distribution can be reparametrised to avoid the use of the constrained parameter \mathbf{V} . From these constraints, define ρ so that $\rho_1 = \rho$, $\rho_2 = 1/\rho$ and $\rho_3 = 1$. Define a new orthogonal frame $\{\tilde{\boldsymbol{\xi}}_1, \tilde{\boldsymbol{\xi}}_2, \tilde{\boldsymbol{\xi}}_3\}$, where:

$$\begin{aligned} \tilde{\boldsymbol{\xi}}_3 &:= \boldsymbol{\mu}/\|\boldsymbol{\mu}\|, \\ \tilde{\boldsymbol{\xi}}_2 &:= (0, 0, 1) \times \boldsymbol{\mu}/\|(0, 0, 1) \times \boldsymbol{\mu}\|, \\ \tilde{\boldsymbol{\xi}}_1 &:= \tilde{\boldsymbol{\xi}}_2 \times \tilde{\boldsymbol{\xi}}_3, \end{aligned}$$

where ‘ \times ’ denotes cross product. Hence, the original eigenvectors can be obtained by rotating this new frame by an angle

$\psi \in (0, \pi]$ about $\boldsymbol{\mu}$, i.e. $\boldsymbol{\xi}_i = \text{Rot}(\psi, \boldsymbol{\mu}) \tilde{\boldsymbol{\xi}}_i$, $i = 1, 2$. We then define $\boldsymbol{\gamma} := (\gamma_1, \gamma_2)$ by:

$$\gamma_1 := [(\rho^{-1} - \rho)/2] \cos 2\psi, \quad \gamma_2 := [(\rho^{-1} - \rho)/2] \sin 2\psi.$$

Consequently, the ESAG distribution for $d = 3$ can be parameterised by $\boldsymbol{\mu} \in \mathbb{R}^3$ and $\boldsymbol{\gamma} \in \mathbb{R}^2$. For a data set $\{\mathbf{x}_i\}_{i=1}^N$, $\mathbf{x}_i \in \mathcal{S}^2$, assumed to come from ESAG, there is no closed-form solution for the ESAG MLE, hence numerical optimisation is needed to solve

$$(\hat{\boldsymbol{\mu}}, \hat{\boldsymbol{\gamma}}) = \arg \max_{(\boldsymbol{\mu}, \boldsymbol{\gamma})} \sum_{i=1}^N \log f_{\text{ESAG}}(\mathbf{x}_i; \boldsymbol{\mu}, \boldsymbol{\gamma}).$$

Regression solution by KLE. Given $\mathcal{D} = \{(\mathbf{x}_{ij}, t_{ij})\}_{j=1}^{M_i}\}_{i=1}^N$, $\mathbf{x}_{ij} \in \mathcal{S}^2$, $t_{ij} \in [0, 1]$, and taking $\mathcal{P}_{\mathcal{M}}$ in (8) to be ESAG, solving the regression problem (8, 9) involves solving for each t the numerical optimisation

$$(\hat{\boldsymbol{\mu}}(t), \hat{\boldsymbol{\gamma}}(t)) = \arg \max_{(\boldsymbol{\mu}, \boldsymbol{\gamma})} \sum_{i=1}^N \sum_{j=1}^{M_i} W_{ij}(t) \log f_{\text{ESAG}}(\mathbf{x}_{ij}; \boldsymbol{\mu}, \boldsymbol{\gamma}).$$

B. The angular central Gaussian distribution on $\mathcal{S}^{d-1}/\mathbb{Z}_2$

Given $\mathbf{y} \sim \mathcal{N}(\mathbf{0}, \boldsymbol{\Lambda})$, $\mathbf{y} \in \mathbb{R}^d$, the directions $\mathbf{x} := \mathbf{y}/\|\mathbf{y}\|$ have an *angular central Gaussian distribution* (ACG) with density [37]:

$$f_{\text{ACG}}(\mathbf{x}; \boldsymbol{\Lambda}) := \frac{\Gamma(\frac{d}{2})}{2\sqrt{\pi^d |\boldsymbol{\Lambda}|}} (\mathbf{x}^\top \boldsymbol{\Lambda}^{-1} \mathbf{x})^{-\frac{d}{2}}, \quad \mathbf{x} \in \mathcal{S}^{d-1}/\mathbb{Z}_2. \quad (16)$$

The ACG is antipodally symmetric, i.e. $f_{\text{ACG}}(\mathbf{x}; \boldsymbol{\Lambda}) = f_{\text{ACG}}(-\mathbf{x}; \boldsymbol{\Lambda})$, which makes it a candidate model for axial data. This distribution is uniquely defined up to scalar multiplication of the parameter $\boldsymbol{\Lambda} \in \text{Sym}^+(d)$, i.e. $f_{\text{ACG}}(\mathbf{x}; \boldsymbol{\Lambda}) = f_{\text{ACG}}(\mathbf{x}; c\boldsymbol{\Lambda})$, $c \in \mathbb{R}^+$, an indeterminacy that can be resolved by imposing that $\text{tr}(\boldsymbol{\Lambda}) = d$.

Consider the spectral decomposition $\boldsymbol{\Lambda} = \mathbf{B}\mathbf{A}\mathbf{B}^\top$, $\mathbf{B} := [\mathbf{b}_{(1)}, \dots, \mathbf{b}_{(d)}] \in \text{SO}(d)$, $\mathbf{A} := \text{diag}(a_1, \dots, a_d)$, with eigenvalues $a_1, \dots, a_d \in \mathbb{R}^+$ in descending order, and corresponding eigenvectors $\mathbf{b}_{(1)}, \dots, \mathbf{b}_{(d)} \in \mathcal{S}^{d-1}$. Then the mean of the ACG distribution is given by $\mathbf{b}_{(1)}$, and a_1, \dots, a_d represent the concentration in the corresponding principal directions. Due to the indeterminacy of $\boldsymbol{\Lambda}$, the eigenvalues are usually normalised so that $\text{tr}(\boldsymbol{\Lambda}) = a_1 + \dots + a_d = d$.

For a sample of axial data $\{\mathbf{x}_i\}_{i=1}^N$, $\mathbf{x}_i \in \mathcal{S}^{d-1}/\mathbb{Z}_2$, the MLE of the parameter $\boldsymbol{\Lambda}$ is defined implicitly as the solution of [37]:

$$\hat{\boldsymbol{\Lambda}} = \frac{d}{N} \sum_{i=1}^N \frac{\mathbf{x}_i \mathbf{x}_i^\top}{\mathbf{x}_i^\top \hat{\boldsymbol{\Lambda}}^{-1} \mathbf{x}_i}. \quad (17)$$

In [37] it is proved that the iterative scheme,

$$\boldsymbol{\Lambda}_{k+1} = d \sum_{i=1}^N \left\{ \frac{(\mathbf{x}_i^\top \boldsymbol{\Lambda}_k^{-1} \mathbf{x}_i)^{-1}}{\sum_{i=1}^N (\mathbf{x}_i^\top \boldsymbol{\Lambda}_k^{-1} \mathbf{x}_i)^{-1}} \mathbf{x}_i \mathbf{x}_i^\top \right\}, \quad (18)$$

starting from $\boldsymbol{\Lambda}_0 = \mathbf{I}$ converges as k increases to the solution $\hat{\boldsymbol{\Lambda}}$ of (17). A practical algorithm is to continue iterating until

$d_{\text{SPD}}(\hat{\mathbf{\Lambda}}_{k+1}, \hat{\mathbf{\Lambda}}_k) \leq \epsilon$, where $d_{\text{SPD}}(\cdot)$ is a metric in $\text{Sym}^+(d)$ and ϵ is a desired small value.

Regression solution by KLE: Given $\mathcal{D} = \{(\mathbf{x}_{ij}, t_{ij})\}_{j=1}^{M_i}\}_{i=1}^N$, $\mathbf{x}_{ij} \in \mathcal{S}^{d-1}/\mathbb{Z}_2$, $t_{ij} \in [0, 1]$, the solution to (9) satisfies

$$\hat{\mathbf{\Lambda}}(t) = d \sum_{i=1}^N \sum_{j=1}^{M_i} W_{ij}(t) \frac{\mathbf{x}_{ij} \mathbf{x}_{ij}^\top}{\mathbf{x}_{ij}^\top \hat{\mathbf{\Lambda}}(t)^{-1} \mathbf{x}_{ij}}. \quad (19)$$

Derivation of this kernelised analogue of (17) is given in Appendix A.

An iterative scheme for finding the solution $\hat{\mathbf{\Lambda}}(t)$ of (19) at a new input $t \in [0, 1]$ is

$$\mathbf{\Lambda}_{k+1}(t) = d \sum_{i=1}^N \sum_{j=1}^{M_i} \left[\frac{K_h(t - t_{ij}) (\mathbf{x}_{ij}^\top \mathbf{\Lambda}_k^{-1} \mathbf{x}_{ij})^{-1} \mathbf{x}_{ij} \mathbf{x}_{ij}^\top}{\sum_{i=1}^N \sum_{j=1}^{M_i} K_h(t - t_{ij}) (\mathbf{x}_{ij}^\top \mathbf{\Lambda}_k^{-1} \mathbf{x}_{ij})^{-1}} \right] \quad (20)$$

Algorithm 1 shows the use of Eq. (20) to learn from a dataset of trajectories on $\mathcal{S}^{d-1}/\mathbb{Z}_2$.

C. The SPD lognormal distribution on $\text{Sym}^+(d)$

The cone $\text{Sym}^+(d)$ of $d \times d$ symmetric positive definite matrices is a manifold whose tangent space at any point can be identified with the vector space $\text{Sym}(d)$ of d -by- d symmetric matrices. When equipped with the log-Euclidean metric, $\text{Sym}^+(d)$ has non-positive curvature and is *geodesically complete* [38]. This means that geodesics between any two points are unique, and any point in $\text{Sym}^+(d)$ can be uniquely mapped to a point in $\text{Sym}(d)$. The nonpositive curvature ensures that, unlike the cases of the other manifolds mentioned in Sec. II, it is possible to define a probability distribution with full support on the tangent space of an arbitrary point without needing to “wrap” its image onto the manifold under the exponential map.

Consider the tangent space at the identity, then a point $\mathbf{X} \in \text{Sym}^+(d)$ with spectral decomposition $\mathbf{X} = \mathbf{B} \mathbf{\Lambda}_1 \mathbf{B}^\top$ is mapped to $\text{Sym}(d)$ by the logarithmic map:

$$\log(\mathbf{X}) = \mathbf{B} \log(\mathbf{\Lambda}_1) \mathbf{B}^\top \in \text{Sym}(d), \quad (21)$$

where $\log(\cdot)$ acts element-wise. The corresponding exponential map for $\mathbf{Y} = \mathbf{B} \mathbf{\Lambda}_2 \mathbf{B}^\top \in \text{Sym}(d)$ is given by:

$$\exp(\mathbf{Y}) = \mathbf{B} \exp(\mathbf{\Lambda}_2) \mathbf{B}^\top \in \text{Sym}^+(d), \quad (22)$$

where $\exp(\cdot)$ acts element-wise.

Since $\text{Sym}(d)$ is a $(\frac{1}{2}d(d+1))$ -dimensional vector space, it is possible to define the *symmetric-matrix normal distribution* as follows:

$$\mathbf{Y} \sim \mathcal{N}_{\text{Sym}}(\mathbf{M}, \mathbf{\Sigma}) \Leftrightarrow \text{vecd}(\mathbf{Y}) \sim \mathcal{N}(\text{vecd}(\mathbf{M}), \mathbf{\Sigma}), \quad (23)$$

where $\mathbf{Y}, \mathbf{M} \in \text{Sym}(d)$, $\mathbf{\Sigma} \in \text{Sym}^+(\frac{1}{2}d(d+1))$, and

$$\text{vecd}(\mathbf{Y}) := \left(\text{diag}(\mathbf{Y})^\top, \sqrt{2} \text{offdiag}(\mathbf{Y})^\top \right)^\top \in \mathbb{R}^{\frac{1}{2}d(d+1)}.$$

We now define the *lognormal distribution* in $\text{Sym}^+(d)$ as follows [38]:

$$\mathbf{X} \sim \text{LN}(\mathbf{M}, \mathbf{\Sigma}) \Leftrightarrow \log(\mathbf{X}) \sim \mathcal{N}_{\text{Sym}}(\log(\mathbf{M}), \mathbf{\Sigma}), \quad (24)$$

where $\mathbf{X}, \mathbf{M} \in \text{Sym}^+(d)$, and $\mathbf{\Sigma} \in \text{Sym}^+(\frac{1}{2}d(d+1))$. Hence, $\mathbf{X} \sim \text{LN}(\mathbf{M}, \mathbf{\Sigma})$ has the following density:

$$f_{\text{LN}}(\mathbf{X}; \mathbf{M}, \mathbf{\Sigma}) := \frac{J(\mathbf{X})}{N_{\text{LN}}} \exp \left\{ -\frac{1}{2} \text{vecd}[\log(\mathbf{X}) - \log(\mathbf{M})]^\top \mathbf{\Sigma}^{-1} \text{vecd}[\log(\mathbf{X}) - \log(\mathbf{M})] \right\}, \quad (25)$$

where the normalizing term is given by $N_{\text{LN}} = (2\pi)^{\frac{1}{2}d(d+1)} |\mathbf{\Sigma}|^{\frac{1}{2}}$, and $J(\mathbf{X})$ is the Jacobian in Eq. (14) of [38].

Due to the simplicity of the definition of the lognormal distribution in (24), the maximum likelihood estimate of the parameters is straightforward. Given a sample of SPD data $\{\mathbf{X}_i\}_{i=1}^n$, $\mathbf{X}_i \in \text{Sym}^+(d)$, this estimation is given by:

$$\hat{\mathbf{M}} = \exp \left(\frac{1}{n} \sum_{i=1}^n \log(\mathbf{X}_i) \right), \quad (26)$$

$$\begin{aligned} \hat{\mathbf{\Sigma}} &= \frac{1}{n} \sum_{i=1}^n \text{vecd} \left(\log(\mathbf{X}_i) - \log(\hat{\mathbf{M}}) \right) \\ &\quad \times \text{vecd} \left(\log(\mathbf{X}_i) - \log(\hat{\mathbf{M}}) \right)^\top. \end{aligned} \quad (27)$$

Regression solution by KLE: Given $\mathcal{D} = \{(\mathbf{X}_{ij}, t_{ij})\}_{j=1}^{M_i}\}_{i=1}^N$, $\mathbf{X}_{ij} \in \text{Sym}^+(d)$, $t_{ij} \in [0, 1]$, the estimate of $\hat{\mathbf{M}}$ and $\hat{\mathbf{\Sigma}}$ for a new input $t \in [0, 1]$ is obtained by inserting kernels in Eqs. (26) and (27), respectively:

$$\hat{\mathbf{M}}(t) = \exp \left(\sum_{i=1}^N \sum_{j=1}^{M_i} W_{ij}(t) \log(\mathbf{X}_{ij}) \right), \quad (28)$$

$$\hat{\mathbf{\Sigma}}(t) = \sum_{i=1}^N \sum_{j=1}^{M_i} W_{ij}(t) \boldsymbol{\tau}_{ij}, \quad (29)$$

where

$$\begin{aligned} \boldsymbol{\tau}_{ij} &:= \text{vecd} \left(\log(\mathbf{X}_{ij}) - \log(\hat{\mathbf{M}}) \right) \\ &\quad \times \text{vecd} \left(\log(\mathbf{X}_{ij}) - \log(\hat{\mathbf{M}}) \right)^\top. \end{aligned}$$

Derivation of Eq. (28) is given in Appendix A.

VI. EXPERIMENTS

In this section, four experiments are presented to test the KLE algorithm. The experiments involve data that comes from the different manifolds introduced in Sec. II. In the first two cases, our results are compared against those obtained with the PbDLlib project [39], [40] which works with GMR. In the experiments involving the Franka Emika Panda arm, the coordinate systems O and E are coincident with the frames O and EE in the LibFranka environment [41]. All values of distances are in meters, while angles are in radians.

A. Trajectories on \mathcal{S}^2 with scalar predictor

Consider the manifold \mathcal{S}^2 which was introduced in Sec. II-A. In this experiment, the KLE method is applied to the problem of trajectory learning on \mathcal{S}^2 . Hence, it is desired to obtain a mean and a dispersion structure for new values of the scalar predictor.

Consider $\mathcal{D} = \{\{(\mathbf{x}_{ij}, t_{ij})\}_{j=1}^{M_i}\}_{i=1}^N$, $\mathbf{x}_{ij} \in \mathcal{S}^2$, $t_{ij} \in [0, 1]$. \mathcal{D} consists of $N = 10$ hand-written demonstrations of the letter B which are projected onto the unit sphere. Each trajectory $i = 1, \dots, 10$ contains $M_i = 100$ time-stamped points. These demonstrations are taken from the dataset available from the PbDLlib project [39].

The KLE algorithm is applied using the ESAG distribution on \mathcal{S}^2 as model. The parameters $\hat{\boldsymbol{\mu}}(t)$ and $\hat{\boldsymbol{\Sigma}}(t)$ are estimated for 100 equidistant values of $t \in [0, 1]$ using $h = 0.01$. The result is shown in the top row of Fig. 4. In order to provide a baseline comparison, the code for Riemannian GMR, available from PbDLlib [39], is run for the same dataset \mathcal{D} . The number of stages for the GMR method is fixed to 10. The results are shown in the bottom row of Fig. 4.

An inspection of Fig. 4 shows that the mean (thick black curve) predicted by the KLE method with ESAG model passes through the data more *centrally* than that predicted by the GMR method. The shape and orientation of the probability level ellipses (yellow curves) predicted by KLE vary more in shape and orientation than those predicted by the GMR, revealing more flexibility in the model.

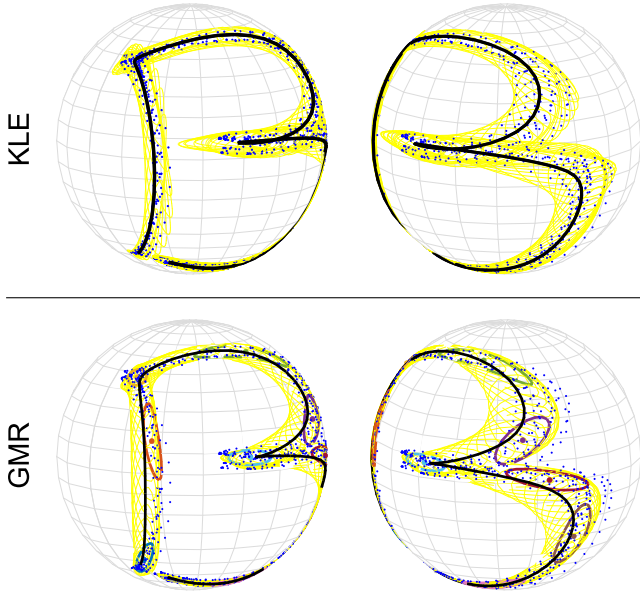


Fig. 4. Regression for trajectories on \mathcal{S}^2 . TOP: KLE method with ESAG model. BOTTOM: Riemannian GMR with 10 stages, the covariance for each stage is shown in coloured thicker curves.

B. Trajectories on $\text{Sym}^+(2)$ with scalar predictor

In order to test learning of trajectories on the manifold $\text{Sym}^+(d)$, which was introduced in Sec. II-D, at a dimension that allows visualization of the data, we consider $d = 2$. It is desired to obtain a mean and a dispersion structure for

new values of the predictor. For this experiment we generate synthetic data, this allows us to have a ground truth against which the results can be compared.

We generate synthetically the set $\mathcal{D} = \{\{(\mathbf{x}_{ij}, t_{ij})\}_{j=1}^M\}_{i=1}^N$, $\mathbf{x}_{ij} \in \text{Sym}^+(2)$, $t_{ij} \in [0, 1]$. For every t_j we simulate the LN distribution, i.e. $\mathbf{x}_{ij} \sim \text{LN}(\mathbf{M}_j, \boldsymbol{\Sigma}_j)$, $j = 1, \dots, N$. By controlling the parameters $\mathbf{M}_j \in \text{Sym}^+(2)$ and $\boldsymbol{\Sigma}_j \in \text{Sym}^+(3)$ we have knowledge of the ground truth.

Consider the spectral decomposition $\mathbf{M}_j = \mathbf{B}(t_j) \text{diag}(a_1(t_j), a_2(t_j)) \mathbf{B}(t_j)^\top$, then $\mathbf{B}(t)$ and $(a_1(t), a_2(t))$ are trajectories in $\text{SO}(2)$ and \mathbb{R}^2 , respectively. We generate $\mathbf{B}(t)$ as planar rotation matrices parametrized by the angle of rotation $\beta(t)$. Then, $\beta(t)$, $a_1(t)$ and $a_2(t)$ require simple scalar interpolation.

Similarly, the decomposition $\boldsymbol{\Sigma}_j = \mathbf{C}(t_j) \text{diag}(b_1(t_j), b_2(t_j), b_3(t_j)) \mathbf{C}(t_j)^\top$ requires the interpolation of scalars $b_1(t), b_2(t), b_3(t) \in \mathbb{R}$, while $\mathbf{C}(t) \in \text{O}(3)$ can be generated by spherical linear interpolation (Slerp) between $\mathbf{C}(0)$ and $\mathbf{C}(1)$.

For this particular experiment, for each of $M = 15$ equidistant t_j we generated $N = 30$ samples. The following scalar interpolations were considered: $a_1(t) = (1 + 9t)^2$, $a_2(t) = (2 - t)^2$, $\beta(t) = 6.6322t - 6.2831t^2$, $b_1(t) = 0.2 + 1.8t$, $b_2(t) = 0.15 + 0.85t$ and $b_3(t) = 0.1$, where $\beta(t)$ was chosen so that $\beta(0) = 0$, $\beta(0.5) = 100\pi/180$ and $\beta(1) = 20\pi/180$. The slerp interpolation for $\mathbf{C}(t)$ was done between $\mathbf{C}(0) = \mathbf{I}_3$ and $\mathbf{C}(1) = \mathbf{R}_Z(15\pi/180)\mathbf{R}_Y(5\pi/180)\mathbf{R}_X(10\pi/180)$.

The first plot from top to bottom of Fig. 5 shows \mathcal{D} . The samples are ellipses which are concentric for each value of t_j and their colour progresses from orange at $t_0 = 0$ to yellow at $t_{15} = 1$. The 15 means \mathbf{M}_j are shown in blue ellipses. We ran the proposed KLE approach with the estimators in Eq. (28) using $h = 0.06$. We computed 30 queries at equidistant values of $t \in [0, 1]$. The results are shown in the second plot of Fig. 5. The estimated mean $\hat{\mathbf{M}}(t)$ is shown in blue ellipses, while the original means, \mathbf{M}_j , are superposed in black outline for comparison. For each request, 30 samples are drawn from $\text{LN}(\hat{\mathbf{M}}(t), \hat{\boldsymbol{\Sigma}}(t))$, their colour progresses from orange (at $t = 0$) to yellow (at $t = 1$).

It can be seen that the estimated $\hat{\mathbf{M}}(t)$ follows the trend in both shape and orientation of original \mathbf{M}_j . The samples drawn from the estimated LN distributions also follow the pattern shown by the training dataset, with an expected slightly larger uncertainty. This uncertainty can be visualised in the bottom plot of Fig. (5), where the eigenvalues of the estimated covariances $\hat{\boldsymbol{\Sigma}}(t)$ (dashed blue curves) are plotted against those of the original $\boldsymbol{\Sigma}_j$. It can be seen that the uncertainty introduced by the sampling from the original distributions, and the regression process perturb the eigenvalues. However, the trend of those still matches the original ones.

We ran the code for Riemannian GMR available from the PbDLlib [39], [40] for the same dataset \mathcal{D} with 10 stages. The results are shown in the third plot of Fig. 5. The estimated mean $\hat{\mathbf{M}}(t)$ is shown in blue ellipses while the original means \mathbf{M}_j are the superposed outlined ellipses. It can be seen that the mean follows the trend almost in a similar way to our approach. However, at the end of the trajectory, the mean is more distorted than the one estimated by KLE. Although the

Riemannian GMR method uses the same LN distribution as model, we were unable to obtain comparable results for the covariance $\hat{\Sigma}(t)$. Hence, its eigenvalues and the samples from the estimated LN distributions are not presented here.

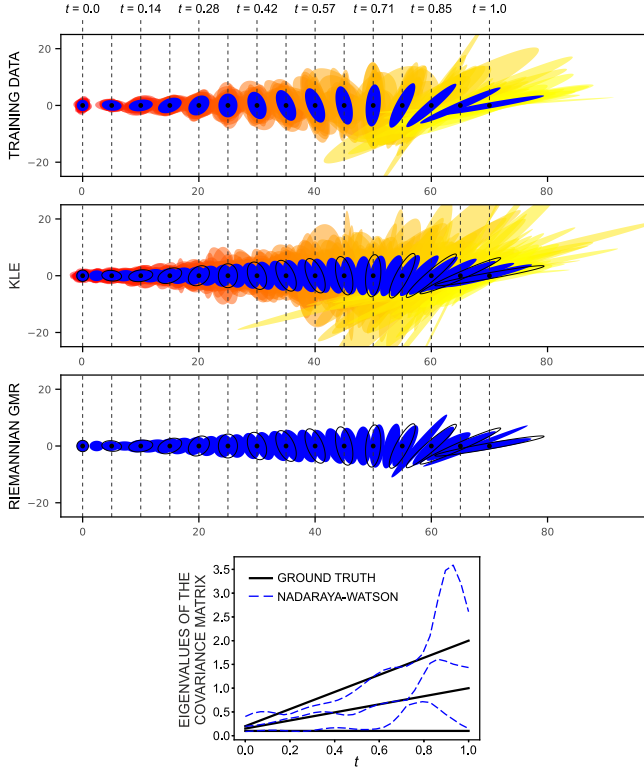


Fig. 5. Learning of trajectories on $\text{Sym}^+(2)$. FIRST PLOT: Training data \mathcal{D} (orange to yellow) and original mean \mathbf{M}_j (blue). SECOND PLOT: Using KLE: estimated mean $\hat{\mathbf{M}}(t)$ (blue), original mean \mathbf{M}_j (black outline), and samples from $\text{LN}(\hat{\mathbf{M}}(t), \hat{\Sigma}(t))$ (orange to yellow). THIRD PLOT: Using Riemannian GMR: estimated mean $\hat{\mathbf{M}}(t)$ (blue), and original mean \mathbf{M}_j (black outline). BOTTOM: eigenvalues of the original covariance matrix Σ_j (solid black), and KLE-computed $\hat{\Sigma}(t)$ (dashed blue)

C. Trajectories on $\text{SE}(3)$ with scalar predictor

In this experiment, we teach a Franka Emika Panda arm with a dustpan attached to its end-effector to drop rubbish into the bin, see Fig. 6 (left). The demonstrated trajectories involve large changes in the orientation of the end-effector frame. We carried out kinesthetic demonstrations (Fig. 6) and tracked the pose of the end-effector frame E in world frame O . Thus, we generate the dataset $\mathcal{D} = \{ \{(\mathbf{x}_{ij}, \mathbf{p}_{ij}, t_{ij})\}_{j=1}^{M_i} \}_{i=1}^N$, where $\mathbf{x}_{ij} \in \mathcal{S}^3/\mathbb{Z}_2$ is the quaternion representation of the orientation, $\mathbf{p}_{ij} \in \mathbb{R}^3$ is the position, and $t_j \in [0, 1]$ is the normalized time. For this experiment, we considered $N = 12$ demonstrations, and we randomly sampled $M_i = 80$, $\forall i$, points from each recorded trajectory.

The left side of Fig. 7 shows the orientation set $\{ \{(\mathbf{x}_{ij}, t_{ij})\}_{j=1}^{M_i} \}_{i=1}^N$. Since \mathbf{x}_{ij} is axial data, we ran a KLE algorithm with an ACG distribution as model. For 200 equidistant values of $t \in [0, 1]$, we estimated the parameter $\hat{\Lambda}(t)$ using the solution for KLE in Eq. (18). We used $h = 0.04$, and the Rao-Fisher metric (see, for example, Eq. (10) in [42]) to stop the iterations in Eq. (18) with a threshold of 1×10^{-4} . Due to

the redundancy of Λ , we normalised it so that $\text{tr}(\hat{\Lambda}(t)) = 4$, $\forall t$. The right-hand side of Fig. 7 shows the mean, $\hat{\mathbf{b}}_{(1)}(t)$, i.e. the eigenvector associated with the largest eigenvalue. In order to have a sense of density levels, for each t , $\text{ACG}(\hat{\Lambda}(t))$ is simulated with 350 samples, then the 140 with the highest density (Eq. (16)) are plotted in Fig. 7. It can be seen that the density follows the trend of the training data.

The left side of Fig. 8 shows the position set $\{ \{(\mathbf{p}_{ij}, t_{ij})\}_{j=1}^{M_i} \}_{i=1}^N$. Since $\mathbf{p}_{ij} \in \mathbb{R}^3$, the task is much simpler and we ran a KLE algorithm with a multivariate Gaussian distribution as model. We used Eq. (14) to determine $\mu(t)$ and $\Sigma(t)$, respectively. The results are shown on the right-hand side of Fig. 8.

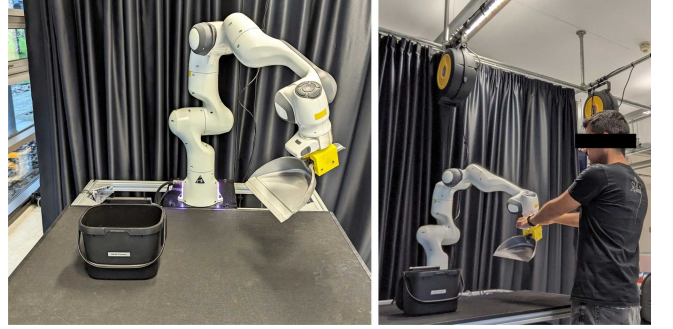


Fig. 6. LEFT: Setup for experiment in Section VI-C – a Franka Panda arm with a dustpan as end-effector, and a bin on the table. RIGHT: A participant carries out a kinesthetic demonstration.

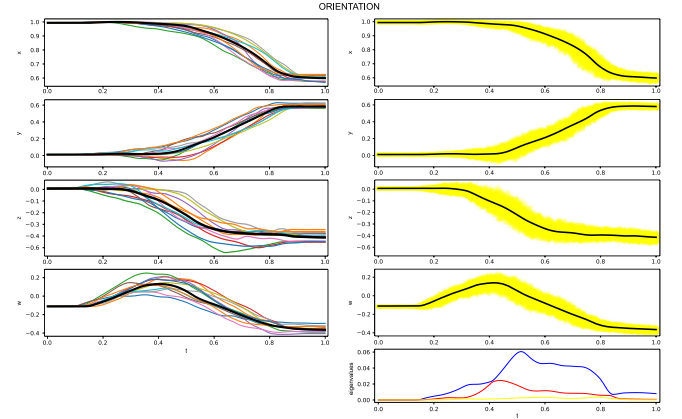


Fig. 7. LEFT: Orientations of demonstrations \mathcal{D} , i.e. dataset $\{ \{(\mathbf{x}_{ij}, t_{ij})\}_{j=1}^{M_i} \}_{i=1}^N$, $\mathbf{x}_{ij} = (x_{ij}, y_{ij}, z_{ij}, w_{ij}) \in \mathcal{S}^3/\mathbb{Z}_2$. RIGHT: Mean $\hat{\mathbf{b}}_{(1)}(t)$ and density level by sampling, see text for details. RIGHT-BOTTOM: second through fourth eigenvalues of $\Lambda(t)$

Fig. 9 shows stills of the robot executing the mean trajectory $\{ \{(\hat{\mathbf{b}}_{(1)}(t_k), \hat{\mu}(t_k), t_k)\}_{k=1}^{200} \}$. Fig. 10 shows several curves generated following the method proposed in Section IV-D. The curves are generated by smoothing through 120 points from the set $\{ \{(\mathbf{x}_k, t_k)\}_{k=1}^{120} \}$, $\mathbf{x}_k \sim \text{ACG}(\hat{\Lambda}(t_k))$, for orientation, and $\{ \{(\mathbf{p}_k, t_k)\}_{k=1}^{120} \}$, $\mathbf{p}_k \sim \mathcal{N}(\hat{\mu}(t_k), \hat{\Sigma}(t_k))$.

It is now desired to adapt the learnt trajectories after the bin has been moved to a new pose. The final pose of the end-effector, ${}^O_E\mathbf{T}^*$, that will allow dropping the rubbish in the bin in its new pose is known. It is known that frame E

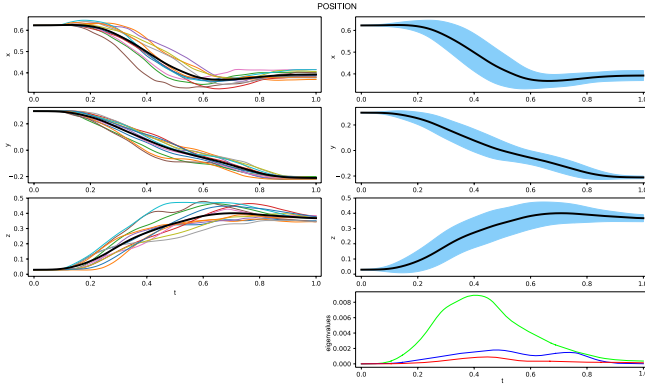


Fig. 8. LEFT: Positions of demonstrations \mathcal{D} , i.e. dataset $\{(\mathbf{p}_{ij}, t_{ij})\}_{j=1}^{M_i} \}_{i=1}^N$, $\mathbf{p}_{ij} = (x_{ij}, y_{ij}, z_{ij}) \in \mathbb{R}^3$. RIGHT: Mean $\hat{\mu}(t)$ with 1.5 standard deviation density level. RIGHT-BOTTOM: eigenvalues of $\hat{\Sigma}(t)$

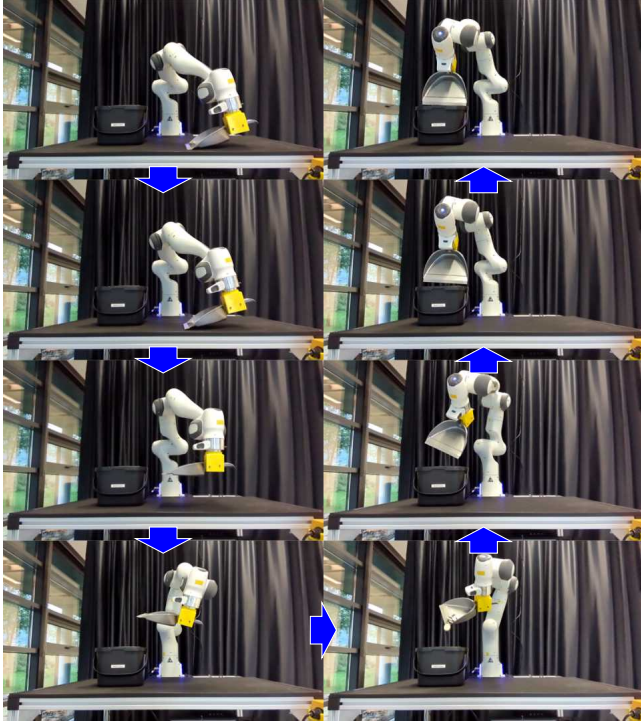


Fig. 9. Franka Panda arm following the mean task-space trajectory obtained from \mathcal{D} . See video in the supplementary material.

must be at a new orientation with quaternion representation $\mathbf{x}_T^* = (0.821, 0.342, -0.243, -0.386)^\top$, and new position $\mathbf{p}_T^* = (0.237, -0.520, 0.343)$. We followed the method presented in Section IV-C. For the orientation part we used activation functions $\alpha(t) = 0.5 - 0.5 \tanh(3t - 2.4)$ and $\beta(t) = 1 - \alpha(t)$. The dataset $\mathcal{E} = \{(\mathbf{y}_{ij}, t_{ij})\}_{j=1}^{80} \}_{i=1}^{12}$ is generated by sampling, for every t_j , $\{\mathbf{y}_{ij}^*\}_{i=1}^{12}$, $\mathbf{y}_{ij}^* \sim ACG(\Lambda^*)$, where $\Lambda^* = \mathbf{B}^* \Lambda (\mathbf{B}^*)^\top$. For a low uncertainty at the adapted point, we set $\Lambda^* = \text{diag}(1 \times 10^5, 1, 1, 1)$. While \mathbf{B}^* is obtained computing an orthonormal basis for the complement space of \mathbf{x}_T^* to \mathbb{R}^4 . The position part is done similarly with samples being drawn from $\mathcal{N}(\mathbf{p}_T^*, 1 \times 10^{-5} \mathbf{I}_3)$, and first activation function $\alpha(t) = 0.5 - 0.5 \tanh(13t - 6.5)$.

The results of this adaptation process are shown in Fig. 11. It can be seen that the means achieve the desired new pose at the end of the trajectory. It can also be seen that the distributions for both position and orientation become highly concentrated at the end of the trajectory. Fig. 12 shows the robot following the adapted mean.

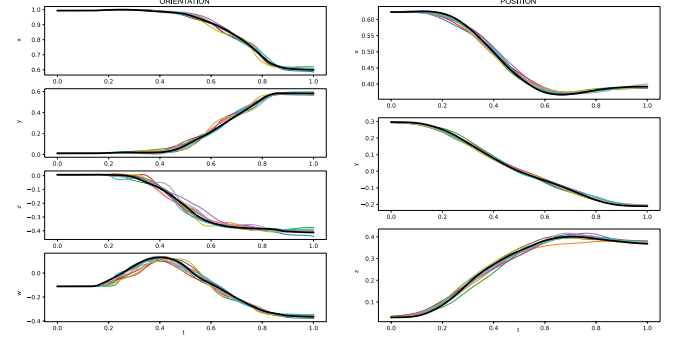


Fig. 10. Ten trajectories generated from the learnt model using the method presented in Section IV-D

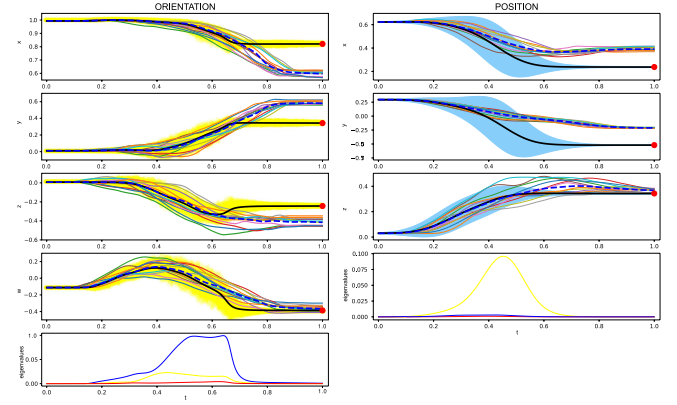


Fig. 11. Adaptation of the learnt trajectories. \mathbf{x}_F^* and \mathbf{p}_F^* are shown in red dots. The adapted mean is shown in thick black curve. The yellow density levels of the orientation part are obtained by sampling, while the ones for position represent 1.5 covariance levels. The original trajectories of \mathcal{D} are also shown as is their mean, in dashed thick curves. The bottom-left plot shows the second through fourth eigenvalues of $\Lambda(t)$, while the bottom-right shows the eigenvalues of $\Sigma(t)$

D. Regression with response in $\text{Sym}^+(6)$ and predictor in $\mathbb{R}^2 \times \mathcal{S}^1$

In this experiment, simple regression (rather than trajectory learning) is carried out using the KLE method. The predictor is on a manifold, $\mathbb{R}^2 \times \mathcal{S}^1$, which represents the position and orientation of a paint roller on a wall, while the response is in $\text{Sym}^+(6)$, representing the manipulability ellipsoid of a demonstrator holding the paint roller. Such manipulability will be then transferred to the robot. This should be reflected in a more human posture.

A 7-DOF Franka Emika Panda arm is to be taught to hold a paint roller against the wall with the manipulability that a human would impose. The demonstrations are a set of postures of a human holding a roller at different positions and orientations of the roller on a wall. For a new position

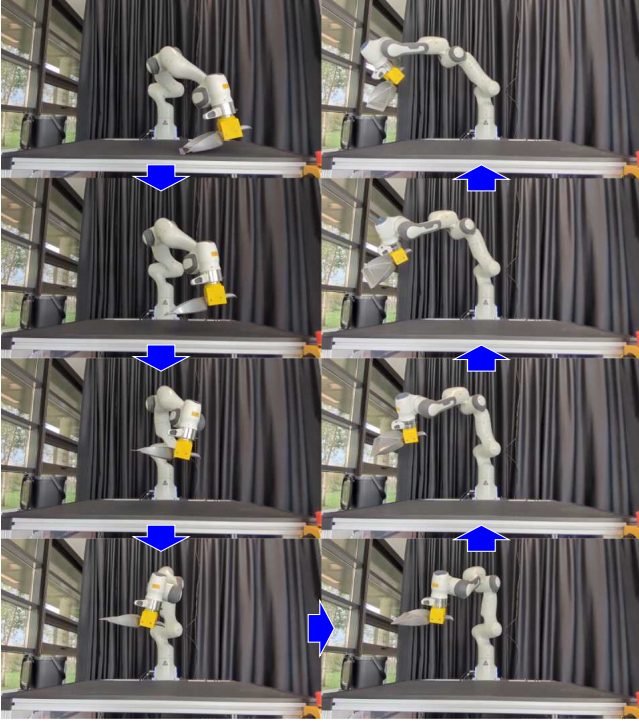


Fig. 12. Franka Panda arm following the adapted task-space trajectory after the bin has been moved. See video in the supplementary material.

and orientation of the roller, it is desired to predict the manipulability ellipsoid that the human would impose and, subsequently, transfer this to the robot. We assume that the angle that the handle of the roller makes with the wall is constant. Therefore, the predictor of this regression problem is in $\mathbb{R}^2 \times \mathcal{S}^1$ (position and orientation of the roller on the wall) and the response is in $\text{Sym}^+(6)$ (manipulability ellipsoid). Since, in this case, the rotation axis of the roller is perpendicular to its translation, $\mathbb{R}^2 \times \mathcal{S}^1$ parametrises the group of planar displacements, $P(3)$ [32]. This is a 3-dimensional subgroup of $SE(3)$ and is sometimes also referred to as $SE(2)$.

Note that, unlike [17] and [18], we are not interested in tracking manipulability from human to robot along a trajectory. Instead, we only aim to transfer the estimated manipulability for a single pose of the end-effector which puts the roller on the wall with a desired position and orientation.

The training dataset for this experiment is $\mathcal{D} = \{(\mathbf{X}_i, \mathbf{p}_i, \phi_i)\}_{i=1}^N$, where $\mathbf{X}_i \in \text{Sym}^+(6)$, $\mathbf{p}_i \in \mathbb{R}^2$, $\phi_i \in \mathcal{S}^1$.

We tracked the right arm of a participant using a Vicon System as shown in Fig. 13 (top). For each demonstration i we obtained the manipulability ellipsoid of the right arm from its Jacobian matrix as $\mathbf{X}_i = \mathbf{J}_{H,i} \mathbf{J}_{H,i}^T$. To obtain $\mathbf{J}_{H,i}$, we use the kinematic model shown in Fig. 13 (bottom). The model is a 7-DOF kinematic chain and was previously used in several publications [43]–[45]. The Vicon world frame V is fixed so that the wall coincides with the y_V – z_V plane. Frame B is the recommended by the International Society of Biomechanics [46] as thorax coordinate system.

Let \mathbf{S}_j be the screw axis of joint j , then the geometry of the kinematic chain modelling the arm is fully defined by the following constraints: \mathbf{S}_1 , \mathbf{S}_2 and \mathbf{S}_3 intersect at C_S , the

shoulder centre. Similarly, \mathbf{S}_5 , \mathbf{S}_6 and \mathbf{S}_7 intersect at C_W , the wrist centre. \mathbf{S}_4 passes through C_E , the elbow centre. \mathbf{S}_1 is antiparallel to y_B , \mathbf{S}_3 is coincident with line $\overline{C_S C_E}$, and \mathbf{S}_2 is perpendicular to \mathbf{S}_1 and \mathbf{S}_3 . \mathbf{S}_5 is coincident with line $\overline{C_E C_W}$, \mathbf{S}_4 is perpendicular to \mathbf{S}_3 and \mathbf{S}_5 . \mathbf{S}_7 is perpendicular to \mathbf{h}_F and \mathbf{h}_P , which are the directions of the middle finger, and the normal to the palm, respectively. Finally, \mathbf{S}_6 is perpendicular to \mathbf{S}_5 and \mathbf{S}_7 .

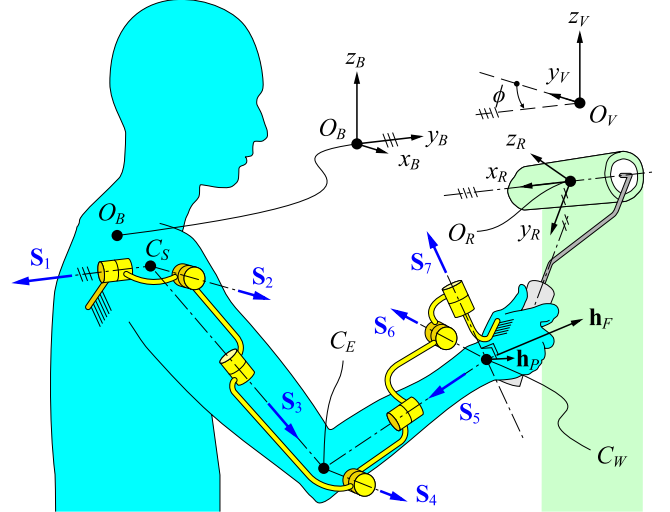
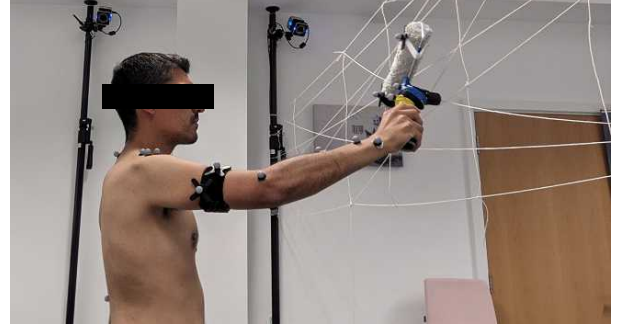


Fig. 13. Data collection for experiment VI-D. TOP: A participant demonstrates how he holds a roller against a wall. The wall is a net of threads to allow the cameras track the markers. The markers set is defined for tracking of the joint centres, and thorax and roller frames. BOTTOM: Kinematic model and related coordinate systems for right arm holding a paint roller.

If $\mathbf{S}_j \in \text{se}(3)$ are the Plücker coordinates of the joint axes [47], the Jacobian matrix is given by $\mathbf{J}_H = [\mathbf{S}_1, \dots, \mathbf{S}_7] \in \mathbb{R}^{6 \times 7}$. We track a frame R fixed to the roller, as shown in Fig. 13. As claimed before, we assume that the angle between axis y_R and the wall, i.e. plane y_V – z_V , is constant. We also assume that the distance between the shoulder centre, C_S , and the wall remains unchanged between demonstrations. Then, our predictor variables $(\mathbf{p}, \phi) \in \mathbb{R}^2 \times \mathcal{S}^1$ are defined as:

- $\mathbf{p} \in \mathbb{R}^2$ is the projection of vector ${}^B \mathbf{r}_{O_R} - {}^B \mathbf{r}_{C_S}$ onto the wall (plane y_V – z_V).
- $\phi \in \mathcal{S}^1$ is the angle between x_R and y_V about $-x_V$.

A total of $N = 80$ demonstrations were obtained. Then the KLE algorithm was used to predict a manipulability ellipsoid for a new pair $(\mathbf{p}, \phi) \in \mathbb{R}^2 \times \mathcal{S}^1$. This is done by modifying the metric in the kernel of Eq. (28). The estimator is then:

$$\hat{\mathbf{M}}(\mathbf{p}, \phi) = \exp \left\{ \sum_{i=1}^N \frac{K_h \left(d_{P(3)}((\mathbf{p}_i, \phi_i), (\mathbf{p}, \phi)) \right) \log(\mathbf{X}_i)}{\sum_{i=1}^N K_h \left(d_{P(3)}((\mathbf{p}_i, \phi_i), (\mathbf{p}, \phi)) \right)} \right\}$$

where $d_{P(3)}(\cdot)$ is a metric in $P(3)$. Just like in $SE(3)$, the lack of a natural length scale in $P(3)$ does not allow for the introduction of a bi-invariant metric. Hence, as suggested in [48], a distance of weighted form is used:

$$d_{P(3)}((\mathbf{p}_i, \phi_i), (\mathbf{p}, \phi)) := w_\phi d_\phi(\phi_i, \phi) + w_p d_p(\mathbf{p}_i, \mathbf{p}),$$

where $d_\phi(\cdot)$ is a metric in \mathcal{S}^1 (smallest angle) and $d_p(\cdot)$ is simply the Euclidean distance in \mathbb{R}^2 . Similarly to [49], we define such weights considering the averages of distances in the rotational and translational data to their respective means:

$$w_p := \left(\frac{1}{N} \sum_{i=1}^N \|\bar{\mathbf{p}}_P - \mathbf{p}_i\| \right)^{-1},$$

$$w_\phi := \left(\frac{1}{N} \sum_{i=1}^N d_\phi(\bar{\phi}, \phi_i) \right)^{-1},$$

where $\bar{\phi}$ is the mean for circular data in Eq. (2.2.4) of [26]. Alternatively, [50] suggests $w_p = 1$ and w_ϕ equal to the largest distance between two points of the projection of the rigid body onto the displacement plane. In our case, such a distance is the axial length of the roller, 0.23m. We tested this metric with very similar results.

It is now necessary to transfer $\hat{\mathbf{M}}(\mathbf{p}, \phi)$ to the robot. Since we are only interested in the proportion and orientation of the manipulability ellipsoid, we normalize the response as $\mathbf{X}_H := \hat{\mathbf{M}}(\mathbf{p}, \phi) / \lambda_{H, \max}$, where $\lambda_{H, \max}$ is the largest eigenvalue of $\hat{\mathbf{M}}(\mathbf{p}, \phi)$.

Since ${}^O_R\mathbf{T}$, the pose of the roller frame R , is fully defined by a requested (\mathbf{p}, ϕ) , and since, once the roller is attached to the end-effector of the robot, the transformation ${}^E_R\mathbf{T}$ is known, then (\mathbf{p}, ϕ) defines a unique pose of the end-effector, ${}^O_E\mathbf{T} = {}^O_R\mathbf{T}(\mathbf{p}, \phi)({}^E_R\mathbf{T})^{-1}$.

After a pose of the end-effector is defined by a requested (\mathbf{p}, ϕ) , the 1-DOF redundancy of the robot gives us one free parameter that allows us to adjust the manipulability ellipsoid of the Franka arm, which we normalise as $\mathbf{X}_F := \mathbf{J}_F \mathbf{J}_F^T / \lambda_{F, \max}$, where $\lambda_{F, \max}$ is the largest eigenvalue of $\mathbf{J}_F \mathbf{J}_F^T$. \mathbf{X}_F is optimised to be as close as possible to \mathbf{X}_H . To this end, we use the analytical solution for the inverse kinematics (IK) of the Franka Panda arm based on [51]. This IK function has as input the end-effector pose, ${}^O_E\mathbf{T}$, and a value of the seventh joint angle, $q_7 \in [q_{7, \min}, q_{7, \max}]$, as free parameter. The function returns a maximum of 8 solutions $\mathbf{q} \in \mathbb{T}^7$. Therefore, for a given ${}^O_E\mathbf{T}$, we consider the Jacobian matrix as a function of q_7 alone. Thus, we are interested in the maximiser:

$$q_7^\# = \arg \min_{q_7} d_{\text{SPD}}(\mathbf{X}_H, \mathbf{X}_F(q_7)), \quad (30)$$

where $d_{\text{SPD}}(\cdot)$ is a metric in $\text{Sym}^+(6)$. For these experiments, we chose the Rao-Fisher metric.

Since this is a 1-dimensional bounded search, the optimization in Eq. (30) can be simply done by discretising $[q_{7, \min}, q_{7, \max}]$, calculating the IK for each angle and picking the one that minimizes (30). Since our IK is analytical, this process is much faster than what it would be if we used any of the numerical IK solvers, which are the commonplace for 7-DOF robots.

We ran the experiment for a requested pose of the roller $(\mathbf{p}, \phi) = ((-0.20, 0.55), \pi/6)$. We set $h = 0.26$ from cross-validation. The estimated \mathbf{X}_H and transferred \mathbf{X}_F have the following eigenvalues:

$$\lambda(\mathbf{X}_H) = (1, 0.821, 0.657, 0.059, 0.035, 0.003),$$

$$\lambda(\mathbf{X}_F) = (1, 0.722, 0.524, 0.058, 0.043, 0.007),$$

with corresponding eigenvectors:

$$\text{eig}(\mathbf{X}_H) = \left\{ \begin{bmatrix} -0.634 \\ -0.457 \\ 0.530 \\ -0.043 \\ -0.206 \\ -0.252 \end{bmatrix}, \begin{bmatrix} -0.765 \\ 0.404 \\ -0.477 \\ 0.039 \\ 0.128 \\ 0.077 \end{bmatrix}, \begin{bmatrix} 0.029 \\ -0.688 \\ -0.608 \\ 0.155 \\ 0.207 \\ -0.298 \end{bmatrix} \right\},$$

$$\text{eig}(\mathbf{X}_F) = \left\{ \begin{bmatrix} -0.025 \\ -0.080 \\ 0.006 \\ 0.855 \\ -0.356 \\ 0.367 \end{bmatrix}, \begin{bmatrix} -0.041 \\ 0.016 \\ 0.347 \\ 0.345 \\ 0.870 \\ 0.034 \end{bmatrix}, \begin{bmatrix} -0.097 \\ -0.384 \\ -0.030 \\ -0.349 \\ 0.120 \\ 0.840 \end{bmatrix} \right\},$$

$$\left\{ \begin{bmatrix} -0.138 \\ -0.095 \\ 0.936 \\ -0.077 \\ -0.298 \\ -0.045 \end{bmatrix}, \begin{bmatrix} 0.985 \\ 0.053 \\ 0.159 \\ 0.019 \\ 0.016 \\ 0.044 \end{bmatrix}, \begin{bmatrix} 0.072 \\ -0.963 \\ -0.074 \\ 0.073 \\ 0.058 \\ -0.229 \end{bmatrix} \right\},$$

$$\left\{ \begin{bmatrix} -0.041 \\ -0.036 \\ 0.056 \\ 0.912 \\ -0.088 \\ 0.392 \end{bmatrix}, \begin{bmatrix} -0.063 \\ 0.077 \\ 0.297 \\ 0.140 \\ 0.926 \\ -0.158 \end{bmatrix}, \begin{bmatrix} -0.031 \\ -0.229 \\ 0.049 \\ -0.370 \\ 0.206 \\ 0.874 \end{bmatrix} \right\}$$

Eq. (30) returned $q_7^\# = 1.412$, with $\mathbf{q}^\# = (-0.886, 1.651, 2.154, -1.528, 2.322, 2.165, 1.412)$ as whole configuration of the arm. The corresponding position and orientation ellipsoids for \mathbf{X}_F and \mathbf{X}_H are shown in Fig. 14.

Fig. 15 shows the Franka Panda arm in a home configuration, \mathbf{q}_0 , from which it moves to the pose ${}^O_E\mathbf{T}$ defined by the requested (\mathbf{p}, ϕ) . We used MoveIt! to plan from \mathbf{q}_0 to the computed $\mathbf{q}^\#$ (Fig. 15, right-top). As a comparison, we then asked MoveIt! to plan from the same home configuration to ${}^O_E\mathbf{T}(\mathbf{p}, \phi)$ (Fig. 15, right-bottom). When compared to the final posture achieved by the task-space MoveIt! planner, it can be seen that the posture $\mathbf{q}^\#$ obtained with our method better imitates the posture that a human would have when holding the paint roller against the wall.

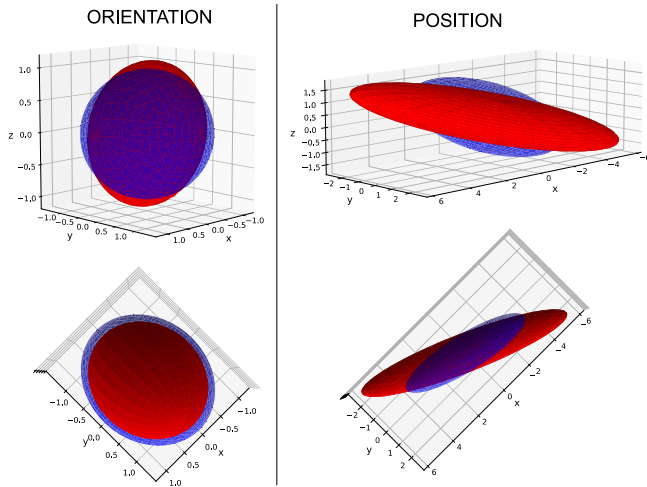


Fig. 14. Position and orientation ellipsoids for \mathbf{X}_H (red) and \mathbf{X}_F (blue)

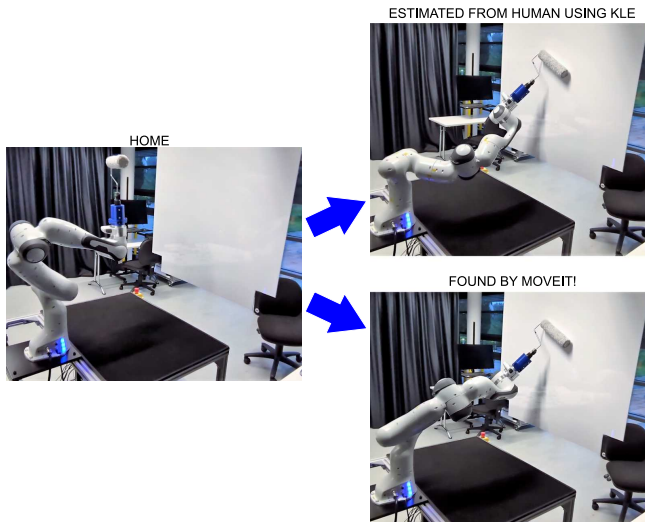


Fig. 15. The Franka Panda arm is initially in a home configuration \mathbf{q}_0 (LEFT). Then $\mathbf{q}^\#$, which optimises \mathbf{X}_F to be as close as possible to $\mathbf{X}_H(\mathbf{p}, \phi)$ is set as *joint goal* on Moveit!. This takes the robot to $\mathbf{q}^\#$ (RIGHT-TOP). Starting again from \mathbf{q}_0 , ${}^O_E\mathbf{T}(\mathbf{p}, \phi)$ is set as *pose goal* on Moveit! which takes the robot to the configuration shown on the RIGHT-BOTTOM. See video in the supplementary material.

VII. CONCLUSIONS

In this paper, the method of kernelised likelihood estimation (KLE) was proposed as a tool for on-manifold LfD. The method is based on the idea of local likelihood, where the terms of the log-likelihood expression of a probability density function are weighted with kernels. The result is a non-parametric regression on the parameters of the probability distribution. Since this concept is independent of the probability model, the learning method can be applied on any manifold as long as the selected probability model has a solution for the maximum likelihood estimation (MLE) for i.i.d. data. This generality allowed us to apply the method to trajectory learning on different manifolds. The learning is probabilistic, meaning that, for a new value of the predictor, we are able to estimate not only the mean of the response, but also the dispersion structure of it. Unlike most of the trajectory

learning methods in robotics, KLE works intrinsically on the manifold, rather than on projections on one or several tangent spaces.

It was shown in the first experiment (Sec. VI-B) that the mean curve computed by our method cross more centrally the data compared to the GMR method. This experiment also showed that the KLE method is applicable even when no simple solution for the MLE is known. In which case Eq. (9) has to be solved directly with a numerical solver. In our second experiment (Sec. VI-B), we used the same probability model employed by GMR, the SPD log-normal distribution. However, our method recovered the mean of the ground truth more precisely than GMR. Our method was also able to recover the covariance matrices of the ground truth. The distortion seen in the results obtained with GMR are a consequence of the projection onto tangent spaces.

In our third experiment (Sec. VI-C), the KLE method was applied to the learning pose trajectories with a large change of orientation. The robot learnt to use trajectories for dropping rubbish into a bin using a dustpan. Adaptation of the trajectories to a new position of the dustpan was achieved. The fourth experiment (Sec. VI-D) shown the application of the KLE method as a regression tool with both predictor and responds lying on manifolds. The task was to teach a redundant robot arm to hold a paint roller against the wall with the manipulability that a human would impose to it.

It is commonly thought that the use of intrinsic probability distributions for manifold-valued data results in intractable algorithms for robot learning. This belief probably stems from the complexity of the normalising term of the Bingham distribution, whose computation is normally done through look-up tables or even neural networks [28]. In this paper, we used the ACG distribution as an alternative to the Bingham distribution. We believe that the advantages of the ACG distribution, namely having a simpler MLE solution and density function, can be further exploited to improve the performance of other learning algorithms.

In future research, we will apply the KLE method to other types of manifold-valued data that were not covered in this paper, for example the Grassmannian manifold. We will also improve the generation of random trajectories from the learnt model using the method proposed in Sec. IV-D, so that the dispersion of sampled curves better reflects the variability of the original demonstrations.

ACKNOWLEDGMENT

This work was supported by UK Research and Innovation (UKRI), CHIST-ERA (HEAP: EP/S033718/2), National Science Foundation (NSF DMS-2015374), and the National Institute of Health (NIH R37-CA214955).

REFERENCES

- [1] A. Ijspeert, J. Nakanishi, H. Hoffmann, P. Pastor, and S. Schaal, "Dynamical movement primitives: learning attractor models for motor behaviors," *Neural computation*, vol. 25, no. 2, pp. 328–373, 2013.
- [2] E. Todorov and M. I. Jordan, "Optimal feedback control as a theory of motor coordination," *Nature neuroscience*, vol. 5, no. 11, pp. 1226–1235, 2002.

- [3] D. Parent, A. Colomé, and C. Torras, "Variable impedance control in cartesian latent space while avoiding obstacles in null space," in *2020 IEEE International Conference on Robotics and Automation (ICRA)*. IEEE, 2020, pp. 9888–9894.
- [4] Q. Cheng, W. Zhang, H. Liu, Y. Zhang, and L. Hao, "Research on the path planning algorithm of a manipulator based on GMM/GMR-MPRM," *Applied Sciences*, vol. 11, no. 16, p. 7599, 2021.
- [5] K. T. Ly, M. Poozhivil, H. Pandya, G. Neumann, and A. Kucukyilmaz, "Intent-aware predictive haptic guidance and its application to shared control teleoperation," in *2021 30th IEEE international conference on robot & human interactive communication (RO-MAN)*. IEEE, 2021, pp. 565–572.
- [6] D. Cohn, Z. Ghahramani, and M. Jordan, "Active learning with statistical models," *Journal of artificial intelligence research*, vol. 4, pp. 129–145, 1996.
- [7] S. Calinon, F. Guenter, and A. Billard, "On learning, representing, and generalizing a task in a humanoid robot," *IEEE Transactions on Systems, Man, and Cybernetics, Part B (Cybernetics)*, vol. 37, no. 2, pp. 286–298, 2007.
- [8] A. Paraschos, C. Daniel, J. Peters, and G. Neumann, "Probabilistic movement primitives," *Advances in neural information processing systems*, vol. 26, 2013.
- [9] Y. Huang, L. Roza, J. Silvério, and D. G. Caldwell, "Kernelized movement primitives," *The International Journal of Robotics Research*, vol. 38, no. 7, pp. 833–852, 2019.
- [10] P. C. López-Custodio, R. Fu, J. S. Dai, and Y. Jin, "Compliance model of Exechon manipulators with an offset wrist," *Mechanism and Machine Theory*, vol. 167, p. 104558, 2022.
- [11] X. Pennec, "Intrinsic statistics on riemannian manifolds: Basic tools for geometric measurements," *Journal of Mathematical Imaging and Vision*, vol. 25, pp. 127–154, 2006.
- [12] S. Said, L. Bombrun, Y. Berthoumieu, and J. Manton, "Riemannian Gaussian distributions on the space of symmetric positive definite matrices," *IEEE Transactions on Information Theory*, vol. 63, no. 4, pp. 2153–2170, 2017.
- [13] Y. Huang, F. Abu-Dakka, J. Silvério, and D. Caldwell, "Toward orientation learning and adaptation in cartesian space," *IEEE Transactions on Robotics*, vol. 37, no. 1, pp. 82–98, 2020.
- [14] W. Wang, M. Saveriano, and F. Abu-Dakka, "Learning deep robotic skills on Riemannian manifolds," *IEEE Access*, vol. 10, pp. 114 143–114 152, 2022.
- [15] M. Zeestraten, I. Havoutis, J. Silvério, S. Calinon, and D. Caldwell, "An approach for imitation learning on Riemannian manifolds," *IEEE Robotics and Automation Letters*, vol. 2, no. 3, pp. 1240–1247, 2017.
- [16] S. Kim, R. Haschke, and H. Ritter, "Gaussian mixture model for 3-DOF orientations," *Robotics and Autonomous Systems*, vol. 87, pp. 28–37, 2017.
- [17] N. Jaquier, L. Roza, D. Caldwell, and S. Calinon, "Geometry-aware manipulability learning, tracking, and transfer," *The International Journal of Robotics Research*, vol. 40, no. 2-3, pp. 624–650, 2021.
- [18] A. Reithmeir, L. Figueredo, and S. Haddadin, "Human-to-robot manipulability domain adaptation with parallel transport and manifold-aware ICP," in *2022 IEEE/RSJ International Conference on Intelligent Robots and Systems (IROS)*. IEEE, 2022, pp. 5218–5225.
- [19] M. J. Zeestraten, I. Havoutis, S. Calinon, and D. G. Caldwell, "Learning task-space synergies using Riemannian geometry," in *2017 IEEE/RSJ International Conference on Intelligent Robots and Systems (IROS)*. IEEE, 2017, pp. 73–78.
- [20] M. Devanne, O. Rémy-Néris, B. Le Gals-Garnett, G. Kermarrec, A. Thepaut *et al.*, "A co-design approach for a rehabilitation robot coach for physical rehabilitation based on the error classification of motion errors," in *2018 Second IEEE International Conference on Robotic Computing (IRC)*. IEEE, 2018, pp. 352–357.
- [21] A. Ude, B. Nemec, T. Petric, and J. Morimoto, "Orientation in cartesian space dynamic movement primitives," in *2014 IEEE International Conference on Robotics and Automation (ICRA)*. IEEE, 2014, pp. 2997–3004.
- [22] L. Koutras and Z. Doulgeri, "A correct formulation for the orientation dynamic movement primitives for robot control in the cartesian space," in *Conference on robot learning*. PMLR, 2020, pp. 293–302.
- [23] M. Saveriano, F. Franzel, and D. Lee, "Merging position and orientation motion primitives," in *2019 International Conference on Robotics and Automation (ICRA)*. IEEE, 2019, pp. 7041–7047.
- [24] L. Roza and V. Dave, "Orientation probabilistic movement primitives on Riemannian manifolds," in *Conference on Robot Learning*. PMLR, 2022, pp. 373–383.
- [25] C. Bingham, "An antipodally symmetric distribution on the sphere," *The Annals of Statistics*, pp. 1201–1225, 1974.
- [26] K. Mardia and P. Jupp, *Directional Statistics*, 1st ed. Wiley Series in Probability and Statistics, 1999.
- [27] S. Riedel, Z.-C. Marton, and S. Kriegel, "Multi-view orientation estimation using Bingham mixture models," in *2016 IEEE international conference on automation, quality and testing, robotics (AQTR)*. IEEE, 2016, pp. 1–6.
- [28] S. James and P. Abbeel, "Bingham policy parameterization for 3d rotations in reinforcement learning," *arXiv preprint arXiv:2202.03957*, 2022.
- [29] J. Staniswalis, "The kernel estimate of a regression function in likelihood-based models," *Journal of the American Statistical Association*, vol. 84, no. 405, pp. 276–283, 1989.
- [30] R. Tibshirani and T. Hastie, "Local likelihood estimation," *Journal of the American Statistical Association*, vol. 82, no. 398, pp. 559–567, 1987.
- [31] S. Calinon, "Gaussians on Riemannian manifolds: Applications for robot learning and adaptive control," *IEEE Robotics & Automation Magazine*, vol. 27, no. 2, pp. 33–45, 2020.
- [32] J. Hervé, "Analyse structurelle des mécanismes par groupe des déplacements," *Mechanism and Machine Theory*, vol. 13, no. 4, pp. 437–450, 1978.
- [33] B. Siciliano, L. Sciacivico, L. Villani, and G. Oriolo, *Robotics: Modelling, Planning and Control*. Springer Publishing Company, Incorporated, 2010.
- [34] E. A. Nadaraya, "On estimating regression," *Theory of Probability & Its Applications*, vol. 9, no. 1, pp. 141–142, 1964.
- [35] G. S. Watson, "Smooth regression analysis," *Sankhya: The Indian Journal of Statistics, Series A (1961-2002)*, vol. 26, no. 4, pp. 359–372, 1964.
- [36] P. Paine, S. Preston, M. Tsagris, and A. Wood, "An elliptically symmetric angular Gaussian distribution," *Statistics and Computing*, vol. 28, pp. 689–697, 2018.
- [37] D. E. Tyler, "Statistical analysis for the angular central Gaussian distribution on the sphere," *Biometrika*, vol. 74, no. 3, pp. 579–589, 1987.
- [38] A. Schwartzman, "Lognormal distributions and geometric averages of symmetric positive definite matrices," *International Statistical Review*, vol. 84, no. 3, pp. 456–486, 2016.
- [39] S. Calinon, "Pbdlb matlab," <https://gitlab.idiap.ch/rli/pbdlb-matlab/>, 2019, accessed: 09-2023.
- [40] —, "A tutorial on task-parameterized movement learning and retrieval," *Intelligent service robotics*, vol. 9, pp. 1–29, 2016.
- [41] Franka Emika GmbH, "Franka Control Interface: Robot and interface specifications," https://frankaemika.github.io/docs/control_parameters.html, 2017, accessed: 09-2023.
- [42] F. Nielsen, "A simple approximation method for the Fisher-Rao distance between multivariate normal distributions," *Entropy*, vol. 25, no. 4, 2023. [Online]. Available: 4
- [43] A. Bertomeu-Motos, A. Blanco, F. J. Badesa, J. A. Barrios, L. Zollo, and N. Garcia-Aracil, "Human arm joints reconstruction algorithm in rehabilitation therapies assisted by end-effector robotic devices," *Journal of NeuroEngineering and Rehabilitation*, vol. 15, p. 11 pages, 2018.
- [44] A. M. Zanchettin, P. Rocco, L. Bascetta, I. Symeonidis, and S. Peldschus, "Kinematic motion analysis of the human arm during a manipulation task," in *ISR 2010 (41st International Symposium on Robotics) and ROBOTIK 2010 (6th German Conference on Robotics)*, 2010, pp. 1–6.
- [45] Q. Li, Y. Xia, X. Wang, P. Xin, W. Chen, and C. Xiong, "Muscle-effort-minimization-inspired kinematic redundancy resolution for replicating natural posture of human arm," *IEEE Transactions on Neural Systems and Rehabilitation Engineering*, vol. 30, pp. 2341–2351, 2022.
- [46] G. Wu, F. van der Helm, H. (DirkJan) Veeger, M. Makhsous, P. Van Roy, C. Anglin, J. Nagels, A. R. Karduna, K. McQuade, X. Wang, F. W. Werner, and B. Buchholz, "ISB recommendation on definitions of joint coordinate systems of various joints for the reporting of human joint motion—Part II: shoulder, elbow, wrist and hand," *Journal of Biomechanics*, vol. 38, no. 5, pp. 981–992, 2005.
- [47] K. Hunt, *Kinematic Geometry of Mechanisms*, ser. Oxford engineering science series. Clarendon Press, 1978.
- [48] F. C. Park, "Distance metrics on the rigid-body motions with applications to mechanism design," *Journal of Mechanical Design*, vol. 117, no. 1, pp. 48–54, 03 1995.
- [49] S. Felton, É. Fromont, and E. Marchand, "Deep metric learning for visual servoing: when pose and image meet in latent space," in *IEEE Int. Conf. on Robotics and Automation*, 2023, pp. 741–747.

- [50] J. M. R. Martinez and J. Duffy, "On the metrics of rigid body displacements for infinite and finite bodies," *Journal of Mechanical Design*, vol. 117, no. 1, pp. 41–47, 03 1995.
- [51] Y. He and S. Liu, "Analytical inverse kinematics for Franka Emika Panda – a geometrical solver for 7-DOF manipulators with unconventional design," in *2021 9th International Conference on Control, Mechatronics and Automation (ICCM)*, 2021, pp. 194–199.
- [52] K. Mardia, J. Kent, and J. Bibby, *Multivariate Analysis*, 1st ed. Academic Press series on Probability and Mathematical Statistics, 1980.
- [53] K. B. Petersen, M. S. Pedersen *et al.*, "The matrix cookbook," *Technical University of Denmark*, vol. 7, no. 15, p. 510, 2008.

APPENDIX A PROOFS

Proof of Eq. (14). The log-likelihood function for a $\mathcal{N}(\boldsymbol{\mu}, \boldsymbol{\Sigma})$ -distributed observation, \mathbf{x}_i , is

$$\ell_i = -\frac{1}{2} \log |2\pi\boldsymbol{\Sigma}| - \frac{1}{2} (\mathbf{x}_i - \boldsymbol{\mu})^\top \boldsymbol{\Sigma}^{-1} (\mathbf{x}_i - \boldsymbol{\mu}), \quad (31)$$

and for an independent sample $\{\mathbf{x}_i\}_{i=1, \dots, N}$ of such observations, the log-likelihood, $\ell = \sum_{i=1}^N \ell_i$, can be written [52]

$$\ell = -\frac{N}{2} \log |2\pi\boldsymbol{\Sigma}| - \frac{N}{2} \text{tr}(\boldsymbol{\Sigma}^{-1} \mathbf{S}) - \frac{N}{2} (\bar{\mathbf{x}} - \boldsymbol{\mu})^\top \boldsymbol{\Sigma}^{-1} (\bar{\mathbf{x}} - \boldsymbol{\mu}), \quad (32)$$

where $\bar{\mathbf{x}} = N^{-1} \sum_{i=1}^N \mathbf{x}_i$ and $\mathbf{S} = N^{-1} \sum_{i=1}^N (\mathbf{x}_i - \boldsymbol{\mu})(\mathbf{x}_i - \boldsymbol{\mu})^\top$. From (32) it follows (see e.g. [52]) that the MLEs of the model parameters are $\hat{\boldsymbol{\mu}} = \bar{\mathbf{x}}$ and $\hat{\boldsymbol{\Sigma}} = \mathbf{S}$.

We consider now the $\boldsymbol{\mu}$ and $\boldsymbol{\Sigma}$ that maximise the weighted log-likelihood, $\tilde{\ell} = \sum_{i=1}^N W_i \ell_i$, where $W_i \geq 0$ and $\sum_{i=1}^N W_i = 1$. We have

$$\tilde{\ell} = -\frac{1}{2} \log |2\pi\boldsymbol{\Sigma}| - \frac{1}{2} \sum_{i=1}^N W_i (\mathbf{x}_i - \boldsymbol{\mu})^\top \boldsymbol{\Sigma}^{-1} (\mathbf{x}_i - \boldsymbol{\mu}), \quad (33)$$

and will define

$$\tilde{\mathbf{x}} = \sum_{i=1}^N W_i \mathbf{x}_i, \quad \tilde{\mathbf{S}} = \sum_{i=1}^N W_i (\mathbf{x}_i - \tilde{\mathbf{x}})(\mathbf{x}_i - \tilde{\mathbf{x}})^\top,$$

as weighted analogues of $\bar{\mathbf{x}}$ and \mathbf{S} , respectively. Using the identity

$$\begin{aligned} & (\mathbf{x}_i - \boldsymbol{\mu})^\top \boldsymbol{\Sigma}^{-1} (\mathbf{x}_i - \boldsymbol{\mu}) \\ &= (\mathbf{x}_i - \tilde{\mathbf{x}})^\top \boldsymbol{\Sigma}^{-1} (\mathbf{x}_i - \tilde{\mathbf{x}}) + (\tilde{\mathbf{x}} - \boldsymbol{\mu})^\top \boldsymbol{\Sigma}^{-1} (\tilde{\mathbf{x}} - \boldsymbol{\mu}) \\ & \quad + 2(\tilde{\mathbf{x}} - \boldsymbol{\mu})^\top \boldsymbol{\Sigma}^{-1} (\mathbf{x}_i - \tilde{\mathbf{x}}), \end{aligned}$$

thus

$$\begin{aligned} & \sum_{i=1}^N W_i (\mathbf{x}_i - \boldsymbol{\mu})^\top \boldsymbol{\Sigma}^{-1} (\mathbf{x}_i - \boldsymbol{\mu}) \\ &= \sum_{i=1}^N W_i (\mathbf{x}_i - \tilde{\mathbf{x}})^\top \boldsymbol{\Sigma}^{-1} (\mathbf{x}_i - \tilde{\mathbf{x}}) + (\tilde{\mathbf{x}} - \boldsymbol{\mu})^\top \boldsymbol{\Sigma}^{-1} (\tilde{\mathbf{x}} - \boldsymbol{\mu}), \end{aligned}$$

and by writing $(\mathbf{x}_i - \tilde{\mathbf{x}})^\top \boldsymbol{\Sigma}^{-1} (\mathbf{x}_i - \tilde{\mathbf{x}}) = \text{tr}(\boldsymbol{\Sigma}^{-1} (\mathbf{x}_i - \tilde{\mathbf{x}})(\mathbf{x}_i - \tilde{\mathbf{x}})^\top)$ it follows that

$$\text{tr} \left\{ \boldsymbol{\Sigma}^{-1} \left[\sum_{i=1}^N W_i (\mathbf{x}_i - \tilde{\mathbf{x}})(\mathbf{x}_i - \tilde{\mathbf{x}})^\top \right] \right\} = \text{tr}(\boldsymbol{\Sigma}^{-1} \tilde{\mathbf{S}}).$$

Hence Eq. (33) becomes

$$\tilde{\ell} = -\frac{1}{2} \log |2\pi\boldsymbol{\Sigma}| - \frac{1}{2} \text{tr}(\boldsymbol{\Sigma}^{-1} \tilde{\mathbf{S}}) - \frac{1}{2} (\tilde{\mathbf{x}} - \boldsymbol{\mu})^\top \boldsymbol{\Sigma}^{-1} (\tilde{\mathbf{x}} - \boldsymbol{\mu}),$$

which is a direct analogue of Eq. (32), except with \mathbf{S} replaced by $\tilde{\mathbf{S}}$, $\bar{\mathbf{x}}$ replaced by $\tilde{\mathbf{x}}$, and differing by the constant factor N ; and consequently it is maximised by

$$\hat{\boldsymbol{\mu}} = \tilde{\mathbf{x}}, \quad \hat{\boldsymbol{\Sigma}} = \tilde{\mathbf{S}}.$$

■

Proof of Eq. (19). The log-likelihood for an $ACG(\boldsymbol{\Lambda})$ -distributed observation, \mathbf{x}_i , is:

$$\ell_i = \log \Gamma \left(\frac{d}{2} \right) - \log 2 \sqrt{\pi^d |\boldsymbol{\Lambda}|} - \frac{d}{2} \log \mathbf{x}_i^\top \boldsymbol{\Lambda}^{-1} \mathbf{x}_i \quad (34)$$

Therefore, with rearrangement of the second term of (34), the weighted log-likelihood of for a set $\{\mathbf{x}_i\}_{i=1}^N$ is:

$$\begin{aligned} \tilde{\ell} &= \log \Gamma \left(\frac{d}{2} \right) - \log 2 \pi^{\frac{d}{2}} - \frac{1}{2} \log |\boldsymbol{\Lambda}| \\ & \quad - \frac{d}{2} \sum_{i=1}^N W_i \log \mathbf{x}_i^\top \boldsymbol{\Lambda}^{-1} \mathbf{x}_i \end{aligned} \quad (35)$$

We wish to obtain the maximiser of $\tilde{\ell}$, thus we set $\partial \tilde{\ell} / \partial \boldsymbol{\Lambda} = \mathbf{0}$, the d -by- d matrix of zeros. From [53], partial derivation of the third term of (35) gives:

$$\frac{\partial}{\partial \boldsymbol{\Lambda}} \log |\boldsymbol{\Lambda}| = (\boldsymbol{\Lambda}^\top)^{-1} = \boldsymbol{\Lambda}^{-1}, \quad (36)$$

while for the contribution of the i th observation to the fourth term of (35) we have:

$$\begin{aligned} \frac{\partial}{\partial \boldsymbol{\Lambda}} \mathbf{x}_i^\top \boldsymbol{\Lambda}^{-1} \mathbf{x}_i &= (\mathbf{x}_i^\top \boldsymbol{\Lambda}^{-1} \mathbf{x}_i)^{-1} \frac{\partial}{\partial \boldsymbol{\Lambda}} (\mathbf{x}_i^\top \boldsymbol{\Lambda}^{-1} \mathbf{x}_i) \\ &= -(\mathbf{x}_i^\top \boldsymbol{\Lambda}^{-1} \mathbf{x}_i)^{-1} \boldsymbol{\Lambda}^{-\top} \mathbf{x}_i \mathbf{x}_i^\top \boldsymbol{\Lambda}^{-\top}. \end{aligned} \quad (37)$$

From (36) and (37), it follows that:

$$\frac{\partial \tilde{\ell}}{\partial \boldsymbol{\Lambda}} = -\frac{1}{2} \boldsymbol{\Lambda}^{-1} + \frac{d}{2} \sum_{i=1}^N W_i (\mathbf{x}_i^\top \boldsymbol{\Lambda}^{-1} \mathbf{x}_i)^{-1} \boldsymbol{\Lambda}^{-\top} \mathbf{x}_i \mathbf{x}_i^\top \boldsymbol{\Lambda}^{-\top}.$$

Hence, by setting $\partial \tilde{\ell} / \partial \boldsymbol{\Lambda} = \mathbf{0}$, it follows that:

$$\begin{aligned} \boldsymbol{\Lambda}^{-1} &= d \sum_{i=1}^N W_i \frac{\boldsymbol{\Lambda}^{-1} \mathbf{x}_i \mathbf{x}_i^\top \boldsymbol{\Lambda}^{-1}}{\mathbf{x}_i^\top \boldsymbol{\Lambda}^{-1} \mathbf{x}_i} \\ \Rightarrow \boldsymbol{\Lambda} &= d \sum_{i=1}^N W_i \frac{\mathbf{x}_i \mathbf{x}_i^\top}{\mathbf{x}_i^\top \boldsymbol{\Lambda}^{-1} \mathbf{x}_i}. \end{aligned}$$

■

Proof of Eq. (28). Since the SPD log-normal distribution is an analog of the multivariate normal distribution with vectorised versions of the logarithms of SPD data, Eq. (28) follows directly from the proof of Eq.(14)

■

Proof of claim in Section IV-D about relation to GPs.

Consider the scalar case $\mathcal{M} = \mathbb{R}$ and $t \in \mathbb{R}$ with $P_{\mathcal{M}}(\theta) = \mathcal{N}(\mu, \sigma^2)$, $\theta = \{\mu, \sigma^2\}$, and let $\mathbf{x}_r = (x_{r,1}, \dots, x_{r,N_r})^\top$, $\hat{\boldsymbol{\mu}} = (\hat{\mu}(t_{r,1}), \dots, \hat{\mu}(t_{r,N_r}))^\top$. Then $\mathbf{x}_r \sim \mathcal{N}(\hat{\boldsymbol{\mu}}, \hat{\sigma}^2 \mathbf{I})$. Let $\mathbf{t} = (t_1, \dots, t_{N_r})$ be chosen times of which to evaluate $\hat{\mu}_r(t)$ and write $\hat{\boldsymbol{\mu}}_r = (\hat{\mu}_r(t_1), \dots, \hat{\mu}_r(t_{N_r}))$. Then, from (13),

$\hat{\boldsymbol{\mu}}_r = \mathbf{S}\mathbf{x}_r$, where \mathbf{S} is the matrix whose (i, j) element, S_{ij} , per (5), equals:

$$S_{ij} = \frac{K_h(t_i - t_{r,j})}{\sum_{j=1}^{N_r} K_h(t_i - t_{r,j})},$$

hence, $\hat{\boldsymbol{\mu}}_r$ is normally distributed for any choice of \mathbf{t}_r . Thus, $\hat{\boldsymbol{\mu}}_r(t)$ is a GP. For the case with $\mathcal{M} = \mathbb{R}^d$, $d > 1$ and $P_{\mathcal{M}}(\theta)$ being the multivariate normal distribution, similar arguments show that $\hat{\boldsymbol{\mu}}_r(t)$ is a GP. ■